Impact of Subsurface Heterogeneities on the CO_2 Storage Potential of Aquifers

NFR KLIMATEK PROGRAM

Intermediate Report

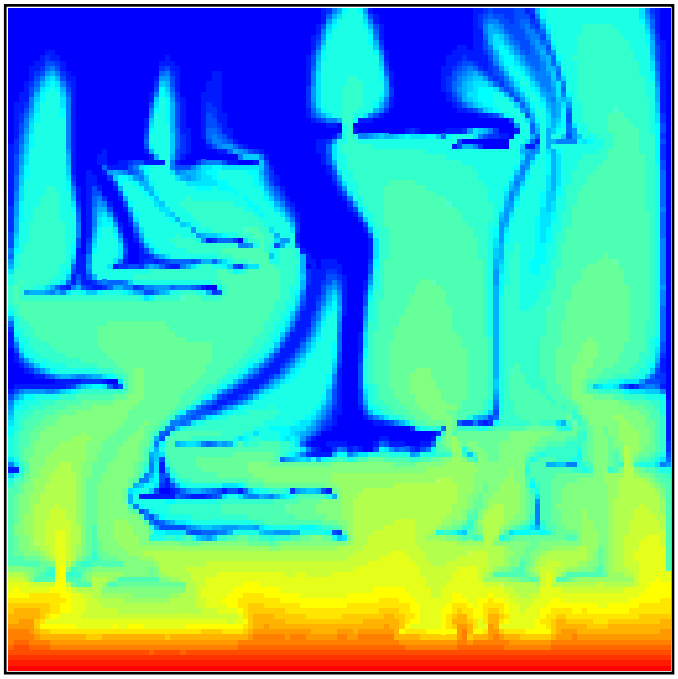

Noelle E. Odling

Nansen Environmental and Remote Sensing Center (NERSC)

Bergen, Norway

February 2000

Introduction

Injection of CO_2 from the Sleipner West platform into the Utsira Formation has been on-going at a rate of around 1 million tonnes per year since October 1996. Petroleum produced from the Sleipner field which lies deeper within the stratigraphic column, contains a high level of CO_2. The CO_2 content is reduced from 9% to 2.5% in order to meeting regulations and the extracted CO_2 is injected via a shallowly dipping well into a salt water aquifer in a sandy section of the Utsira Formation at a depth of 987m below sea level (Fig.1). This represents the first attempt on an industrial scale to dispose of CO_2 to a sub-sea aquifer and represents a unique chance to increase the knowledge on this method of CO_2 disposal and its impact on the environment.

In 1997 research activities through a number of projects were initiated to investigate and monitor the behaviour and migration of the injected CO_2 and its interaction with the aquifer sediments and fluids. These activities are co-ordinated by Statoil in Trondheim, Norway and involve a large number of partners in the industrial and research sectors including the energy companies Statoil, BP Exploration, Mobil Norway, Norsk Hydro and Vattenfjall AB, and the research institutes BGS (UK), BRGM (France), IFP (France), GEUS (Denmark), IKU (Norway), NERSC (Norway), TNO (Netherlands) and IEA-GHG. Funding comes from the energy companies, EU Thermie program, and national research councils.

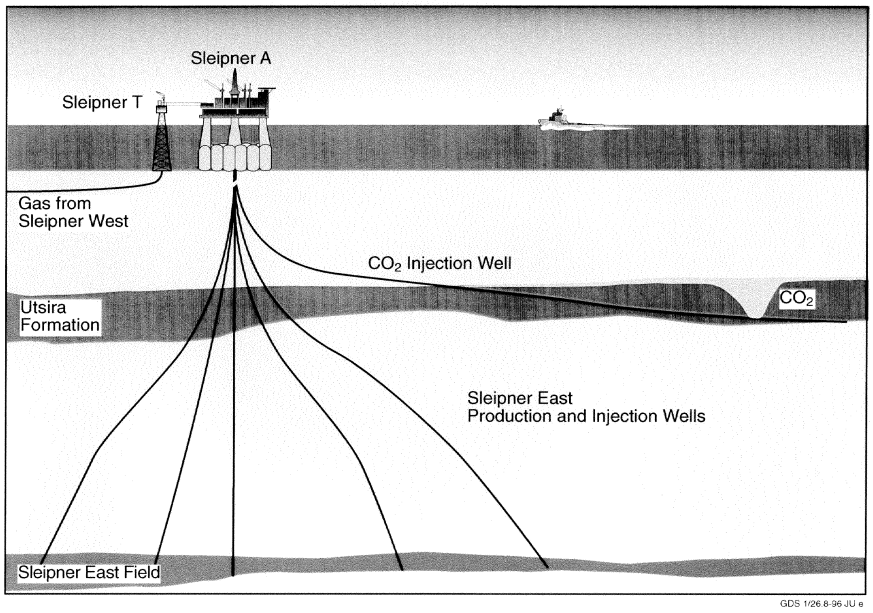

Fig.1 Cross-section showing the Sleipner field and Sleipner A platform. CO_2 removed from produced oil is re-injected into a salt water aquifer in the Utsira Formation

Activities started with an initiation project, SACS Zero Phase, in which a thorough data search and preliminary studies were carried out. This was followed by the SACS project (Saline Water CO_2 Storage) from (01.11.1998 to 31.10,1999) and by SACSII which started 01.03.2000 and is of 2 years duration, both funded through the energy companies and the EU Thermie. The SACS projects have associated with them a number of nationally funded projects including two through the Klimatek program of NFR in Norway. These include the Klimatek project reported here entitled 'Impact of Subsurface heterogeneity on the CO_2 storage potential of aquifers' which is of 12 man months duration over the two year period 01.01.1999-31.12.2000.

The project comprises a study, through numerical modelling, of the influence of rock heterogeneity in aquifers on the behaviour of injected supercritical CO_2. Heterogeneity types present in the Utsira Formation are identified. Flow of CO_2 in the aquifer is simulated with a two phase flow model which can reproduce the complex saturation distributions and fluid fronts resulting from the large viscosity contrast between supercritical CO_2 and water. The model is then used to test the sensitivity of injected CO_2 behaviour to rock heterogeneities, and to determine bulk rock permeabilities and pseudo functions (relative permeabilities for CO_2 and water) for large rock volumes, parameters that can be used as input to a large scale flow simulator. The objectives of the project are:

1) To model the time dependent evolution of the distribution and dissolution of supercritical CO_2 injected into heterogeneous aquifers

2) To assess the potential impact of rock heterogeneity types expected in the Utsira Formation on the behaviour of injected supercritical CO_2

3) To determine the sensitivity of injected CO_2 behaviour to different types of rock and sediment heterogeneity

4) To determine effective bulk permeabilities and pseudo functions (relative permeabilities) for volumes of rock and sediment with sizes comparable to grid blocks used in large scale flow simulations

5) To use scaled up permeability and pseudo functions as input to a large scale flow model of CO_2 injection, with the aim of assessing the importance of accounting for the effects of rock and sediment heterogeneity on the behaviour of injected supercritical CO_2.

This report constitutes an intermediate report on the work done during the first half of the project and concentrates on the impact of heterogeneities of a sedimentary nature on the migration of injected CO_2 in the supercritical phase, contributing to objectives 1) to 4).

The Utsira Formation and the Utsira Sand

Regional Geology

The Cenozoic stratigraphy of the North Sea has been described by several authors (e.g. Degan and Scull 1977, Isaksen and Tonstad 1989, Jordt et al. 1995, Gregersen et al. 1997, 1998, Eidvin et al. 1999) and more recently in detail in a number of reports produced in connection with the SACS project (Lothe and Zweigel 1999, Torp 1999). The Utsira Formation forms the basal part of the Cenozoic dominantly argillaceous Nordland Group (Gregersen et al. 1997) which was deposited in the Mid-Miocene and lies largely in the Norwegian sector of the Southern Viking Graben between the Jaren High and the Tampen Spur, see Fig.2. It forms an elongated sub-crop trending N-S about

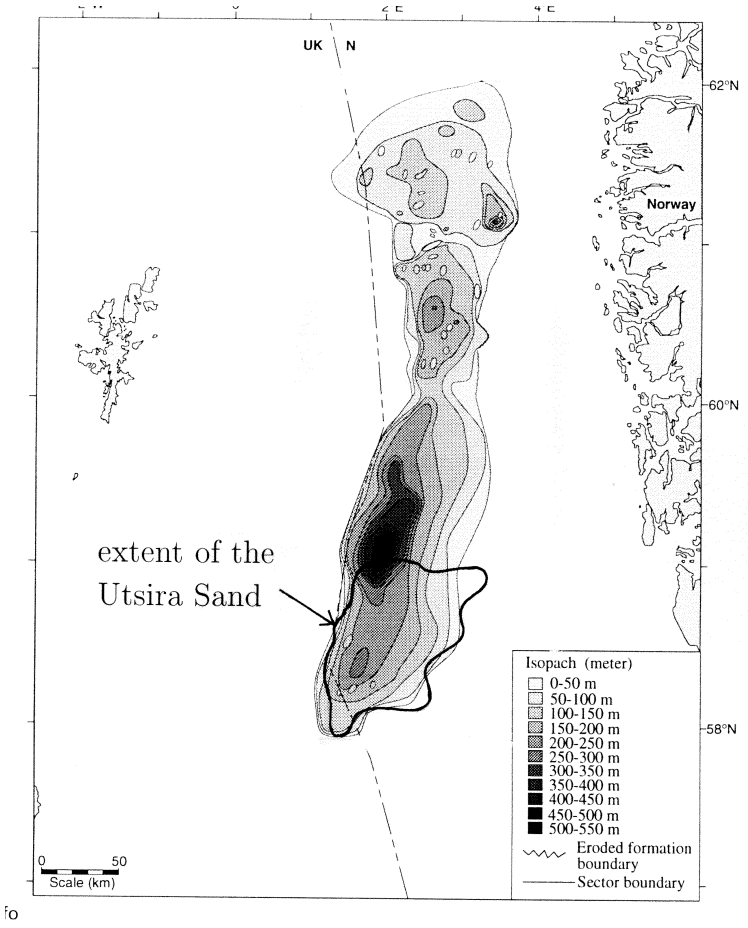

Fig2. The extent of the Utsira Formation and the Utsira Sand in the Northern North Sea (modified from Gregersen 1997).

430 km long and around 85 km wide. It contains two main depo-centres, north and south of 60^{o} N and reaches a maximum thickness of 550m. The Utsira Formation can be traced laterally into the Hutton sands in the British sector. It contains thick sand bodies in its central portions which grad into more shale rich sediments at the margins. The Utsira Formation is over-lain by the shale rich members of the Nordland Group of Pliocene age which down-lap on the top of the Utsira

Formation. This sequence is dominated by prograding sequences with sediment transport from the Norwegian shelf to the W and NW.

Detailed Geology of the Utsira Formation and the Nordland shales at Sleipner

In the Sleipner area, more detailed interpretation of seismic data has revealed that the sands into which CO_2 is being injected form a restricted sand body within the Utsira formation which has been termed the 'Utsira Sand'. The Utsira Sand sub-crops over an area of 12 by 9 km in the Sleipner area (Lothe and Zweigel 1999, Torp 1999) at the location where the Utsira Formation is at its thickest, see Fig.2. This unit has a maximum depth of around 300m and grades into more shale rich sediments on all sides. At the location of the injection well the Utsira Sand has a thickness of 200m.

Detailed analysis of seismic data, well logs and some core have revealed information about the Utsira Sand and the Nordland shale in the vicinity of the Sleipner area (Lothe and Zweigel 1999, Torp 1999). The top and base of the Utsira Formation form strong seismic reflectors and abrupt changes in electrical logs reflect sharp transitions from sand rich to clay rich sediments. Toplap regionally to the west onto the base reflector of the Utsira Sand suggest it represents an erosional boundary (the Miocene unconformity). The top of the Utsira Formation forms the base of prograding units of the Nordland shales which onlap from east and west towards the depo-centre of the Utsira Sand. In the Sleipner area, the base Utsira forms an elongate depression trending NW-SW steepening to the SW. The Utsira Sand is thickest north of the injection site and thins westwards from the injection well showing that this area lies on the western flank of the Utsira Sand unit.

The overlying Pliocene Nordland shales shows rather uniform thickness in the vicinity of the injection well. Here there is a sand wedge of around 16m thickness separated from the Utsira Sand by 5m of shale but does not appear to be connect to the Utsira Sand anywhere. Log cuttings indicate that, apart from this sand wedge, these sediment represent a continuous clay sequence. In the area of the injection site the Pliocene sediment package is around 230 m thick. Seismically, the Utsira Formation shows internally parallel continuous to discontinuous layering. Internal features of gamma and resistivity logs are though to reflect thinning upwards sequences but signs of coarsening upward cycles are also seen. Locally high gamma and resistivity values within the Utsira Sand are thought to reflect clay layers around 1m thick or less. Four of these clay layers could be traced locally from well to well but correlations over distances of over 2 km are not possible. In the injection well (in which resolution is highest due to the deviated nature of this well) some 14 of these shale layers were detected. Limited resolution of the electrical logs means this number is a minimum and additional thinner shale and clay layer may be present.

The base of the Utsira Sand shows mounds over-lain by onlapping or downlapping layering. These mounds show generally elongated forms, 1-2 km across and are interpreted as mud volcanoes formed by mud diapirism sourced by the underlying Hordaland shales. The bulk of mud diapirism seems to have taken place after the deposition of the Utsira sands and to have formed mud sheets within the lower parts of the Utsira Sand. The top of the Utsira Sand is often depressed over these mounds thought to be caused by the greater compaction of the clay forming these mounds. They seem also to associated with disturbed areas on seismic section interpreted as gas chimneys formed by the upward migration of natural gas (Heggland 1997). This is corroborated by mud-log reports of shallow gas in the Utsira Formation and overlying shales. Mud volcanoes development may

have been triggered and/or formed preferential routes for the migration of natural gas. In the overlying shales, high seismic amplitudes (reflecting shallow gas occurrence) show a weak NW-SE alignment which may reflect a structural pattern such as small scale faults or joints which may have controlled gas migration.

Petrography

The only core material available is from well 15/9-A23 (sampled at 905.4-910.8 TVD from the Utsira Sand) which has been analyzed by IKU (Norway), GEUS (Denmark) and BGS (UK) (Lothe and Zweigel 1999, Torp 1999). This is composed of grey, very fine grained, moderate to well sorted sand. The sediment is rather homogeneous without internal structures and contains shell and rock fragments. Grains are angular to sub-angular with a few rounded grains. Modal analysis gives porosities in the range 27-31%. The sand has a high content of quartz (77-85%) and is little cemented (minor amounts of chlorite cement). Cuttings from several wells in the Sleipner area show that the Utsira Sand varies from very fine to medium coarse sand which is largely poorly cemented. Occasionally fragments of greenish grey claystone are seen but clay is under-represented in cuttings as most clays are washed out but the high content of pyrite indicates the presence of shales. Cuttings from the Nordland shale overlying the Utsira Sand consists of quartz (23-36%) plagioclase (8-15%), and clay minerals (40-60%). The clay minerals consist of mica/illite (18-30%), mixed layer clays (5-15%) and kaolinite (7-16%).

Depositional Environment

Gregersen et al (1997) interpret the Utsira Formation as representing basinal stacked lowstand fan deposits basinward and transgressive highstand deposits landward. Other earlier interpretations include shallow marine tidal sand ridges (Buller et al. 1982, Rundberg 1989, Isaksen and Tonstad 1989) thick stacked barrier island sands inter-layered with lagoonal clays. The Pliocene shales are believed to represent lowstand sequences in the basal parts over-lain by thicker transgressive highstand sequences (Gregersen et al 1997). Information on water depth of deposition is rather contradictory. Minimum water depth from depth reconstructions and decompaction algorithms give a minimum water depth for the Utsira sands of 100m and 250m for the top of the lower Pliocene shale unit (Lothe and Zweigel 1999). This, however, contrasts with estimates of 30-100m from Eivind et al (1999)based on palaeoenvironmental data. More recent estimates of water depth made from microfossils in a sample from well 15/9-A23 (Wilkinson I.P. 1999) suggest middle to outer shelf water depths at the time of deposition (100-200m). These recent estimates on water depths, although spanning a range from 30 to 300m, favours a deeper water marine fan system over a shallow marine tidal environment.

Such marine fan deposits are typically composed of turbidite sequences. The lack of bedding plane structures in the core suggests a chaotic deposition process and the high quartz content indicates mature sediments with possibly long transport distances or reworking, both of which are consistent with sediments laid down by turbidity currents. The Utsira Sand appears to grade laterally into shales over about 70 km. This is consistent with 'lobe' structures (see below) found in many ancient and modern marine fan systems whose sediments are dominated by turbidites.

Turbidites

The ‘most likely environment of the Utsira Formation is thought to be marine fans composed of turbidites and related sediments. Marine fans form major sedimentary structures in marine basins and are frequently found off-shore from large rivers and their deltas and can form large prisms of sediment up to 1 km thick extending laterally several 100’s of kilometres, see Fig.3. They are built up by a number of sedimentary processes which include rock falls, sediment slides, debris flow and turbidity currents (Stow 1992). Sediment slides comprise the bodily movement of sediments on a fluidized basal shear plane. Debris flows consist of slurry like sediment-water mixtures with laminar flow that move on a fluidized basal shear zone. Turbidity currents are density currents of relatively dilute sediment-water mixtures where the sediment is maintained in suspension by turbulent flow. These currents are capable of transporting sediment over very long distances (1000’s km) down very low slopes (less than 1 degree) without significant erosion or deposition and are a major supplier of sediments to the deeper parts of ocean basins. They may form either channelized flows around 1 km wide and 10’s km long or laterally unconfined slope flows. These sedimentary processes build up large fan structures with distinctive sedimentary structures, see Fig.3.

A good summary of turbidite morphology is given by Walker (1978). The typical rock types found in sub-marine fans are 1) classic turbidites, 2) massive sandstones, 3) pebbly sandstones, 4) clast supported conglomerates and 5) matrix supported sediments. The first four are deposited by currents where turbulence was important in supporting the sediment. In the fifth class, fluid turbulence is much less important.

Classic turbidites

The distinctive features of classic turbidites are very parallel bedding with regular alterations of sandstone and shale normally without channeling or major lateral changes in bed thickness for 100s to 1000s m. They are characterized by a number of distinctive features including erosional marks associated with the sharp base of the sandstone beds (sole marks), a suite of internal structures in the sandstone beds (graded bedding, horizontal lamination and ripple cross-lamination) and a pelitic layer on top of each sandstone. Bouma (1962) divided classic turbidite beds into divisions A to E. Division A consists of massive sandstones, B of medium to fine grained sandstones with horizontal laminations, C of sandstones with ripple cross laminations and convolution, D of horizontal laminations of silt and clay, and E, a layer of structure-less silt or clay. Each division of the Bouma sequence represents progressively waning currents upward through the bed. Turbidity currents also wane in their journey across the basin floor. Near their source, turbidites tend to begin with A, with B further from the source and C in the most distal parts. Turbidites in the area of initial deposition (proximal turbidites) also tend to be thicker bedded (20-30 cm), coarser grained (medium sand or coarser), have a higher sand/shale ratio. Finer, thinner bedded turbidites beginning with B or C divisions can indicate distal parts of the system or areas on channel levees.

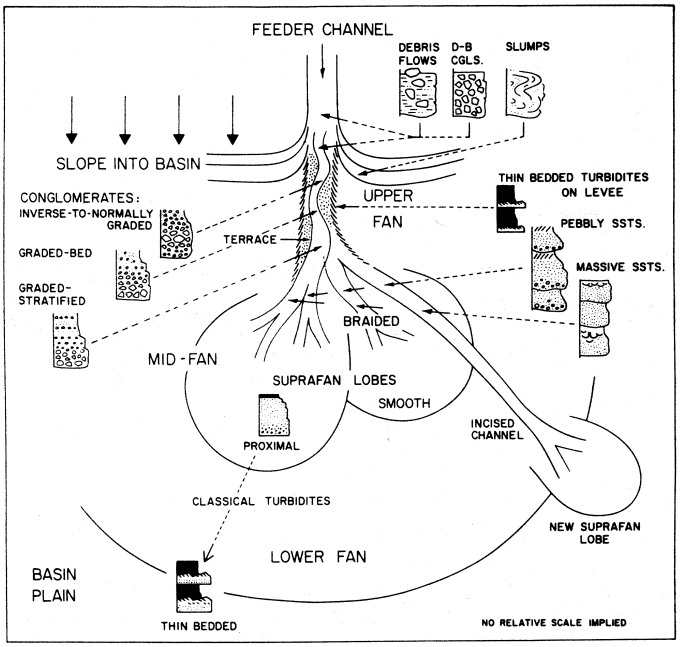

Fig.3 Sketch of submarine fan morphology and sediment types (after Walker 1978).

Massive Sandstones

Classic turbidites can grade laterally into massive sandstones composed of A division beds alone. Beds are typically 0.5 to 5m thick and may be composite. Internally beds are often ungraded and the major internal sedimentary structures are vertical interganular fluid escape tubes and dish structures (thin, sub-horizontal flat to concave upwards argillaceous laminations) which formed during fluid escape.

Pebbly Sandstones

Beds range from 0.5 to over 5m thick and are characterized by sharp bases and an absence of shaley layers. Internal sedimentary features are stratification and cross-stratification. Stratification consists of alternating pebble-rich and pebble-poor layers with gradational bases and tops. Average layer thickness is 5-10 cm. Cross-stratification consisted of sets most commonly around 5 cm high with trough or planar cross-bedding. Pebbly sandstone are commonly lenticular and show scoured bases. Many formations are 10’s to 1000’s m thick built up of many graded beds.

Clast Supported conglomerates

Individual beds range from 1m to over 50m thick, have sharp commonly channelized bases and tend to be laterally impersistent. Shale layers are very uncommon. Beds may show normal or inverse graded bedding or massive bedding. Imbrication of pebbles is common.

Matrix-supported Beds

This sediment type is typical of debris flows. Beds tend to be irregular and lack scour marks. Internally beds are chaotic and resemble tillites. The clast-support mechanism is matrix strength and large clasts can float in the upper parts of the flow often projecting up from the top of the bed.

It is well established that classic turbidites form a complete gradation between thin-bedded (CDE) to proximal (ABCDE) types. Gradation also occurs between classic turbidites and massive sandstones where the loss of bedding regularity is due to increased amounts of scouring and channelization. Pebbly sandstones and clast supported conglomerates probably represent a different depositional mechanism and are thus a distinct lithology from classic turbidites.

Relation of facies to fan morphology

In the upper fan there is a single channel that may have a meandering channel within it, flanked by flat terraces with levee deposits. The middle fan is built up by the deposition of supra-fan lobes which shift position with time. The inner parts of the lobes are composed of shallow braided channels with no levees, while the outer parts are smooth and grades into the lower fan region. The basinal plain and lower fan regions are smooth low-gradient areas with hemipelagic deposition and occasional turbidity currents. Sediments are thin and parallel bedded classic turbidites which become thicker towards the middle fan. Proximal turbidites with monotonous inter-layered sandstones and shales can form on the outer parts of supra-fan lobes. In the supra-fan lobes, deposition within braided channels gives rise to massive sandstones characterized largely by lenticular bedding and shallow channels. Small turbidity currents in the channels may deposit classic turbidites within them. In the upper fan, conglomerates deposited in the channels and perhaps on the terraces are the dominating lithology. Feeder channels can be 10's to 100's m deeps and 100's m to kilometres wide while channel levees are composed of fine grained thin sandstones and mudstones (thin-bedded turbidites). Channels can be plugged with coarse material, such as debris flows and conglomerates, or by very fine materials such as clays and mudstones.

Stratigraphic evolution of fans

In a pro-grading fan sequence, the changing sedimentation environment will lead to a sequence of lithologies from different parts of the fan. Progradation of the lower fan leads to classic turbidites with sandstones beds that become coarser and thicker up-section. Above this are the middle fan sediments where classic turbidites give way to massive or pebbly sandstones. Bed thickness, grain size and sand/shale ratio all increase upwards. Shifting of sediment channels and deposition lead to fining upward sequences in individual lobes ending with the deposition of fine grained mudstones over the abandoned fan. Fining and thinning upwards sequences can be developed in the supra-fan channels, as channels are abandoned with time. Thus, the overall stratigraphy developed during a period of progradation consists of one major coarsening upward sequence with smaller coarsening upward sequences in the lower part and fining upward sequences in the upper part.

The Utsira Formation

Seismic studies by Gregersen (1997, 1998) have identified a number of large scale lens like bodies and a channel feature leading to the interpretation of the Utsira Formation as a sub-marine fan

structure. In the area of the Sleipner platform, available information appears to suggest that the Utsira Sand is dominated by sands. Bore hole logs, however, show that there are also a number of shale layers which can be followed on seismic over distances of 2 km. Samples from the only core available are of a fine, well-sorted sand without visible internal sedimentary structures. This may represent massive sandstones of a channel fill, for instance. If the Utsira Formation is sand dominated, as available information suggests, then the most appropriate interpretation of the Formation may be as middle fan deposits composed largely of channel fill sands. The laterally continuous shale layers which can be traced on seismic may then represent hemipelagic layers deposited when supra-fan lobes and their channels were abandoned as sites of deposition. As sub-marine fan deposits, the sediments are likely to be heterogeneous and contain a number of possible sedimentary structures on a variety of scales that could have an impact on fluid flow and the migration of injected CO_2. On a large scale these include the laterally continuous shale layers are likely to form barriers to upward migration. On the scales of 10s m, heterogeneities include the inter-layering of sands and clays/shales of classic turbidite sequences, and the mixtures of massive sandstones and turbidite sequences expected in channel fills. On a small scale (10's cm to 1 m), internal structures such as ripple cross-bedding and dish-structures could impact on fluid pathways.

Permeability and porosity of sands and clays.

The heterogeneities that may be present in the Utsira Formation and the Nordland Shales which over lie it, result in heterogeneous permeability and porosity fields which will exert an important control on the transport and dispersion of injected CO_2. Of major importance to the modelling of CO_2 injection is therefore the range of permeabilities and porosities that can be expected in the Utsira Sand and overlying shales. From limited core and cuttings the Utsira Sand appears to be either completely or very poorly consolidated. The permeability of the sediments will therefore be close to their at a maximum since there is little compaction or cementing material in the pore space. Measurements of permeability from core material conducted by GEUS give values of 800 to 1450 mD at 39% porosity and by one measurement by IKU gives a permeability of 3D at a porosity of 35% (Torp 1999). The high permeability values emphasis the poor consolidation and lack of compaction in the Utsira Sand. To help assign relevant permeabilities and porosities to models for the heterogeneities that could be present in the Utsira Sands, an overview of permeability and porosity in sands and shales and their major controlling factors is presented.

Permeability and Porosity of Sands

The permeability and porosity of unconsolidated sands depends on grain size, sorting and degree of compaction and consolidation and cementation (e.g.Fetter 1988). Generally, for a give consolidation state, permeability increases as grain size increases but decreases as sorting becomes poorer (i.e. as the spread in grain sizes increases). Porosity is controlled by the size and frequency of pores but permeability is controlled chiefly by the pore throat size. This leads to a complex relationship between porosity and permeability that is not easy to predict. For a sand composed of a constant grain size, permeability increases as the grain size increases (porosity however stays constant) because the pores and pore throats increase in size. However, when a wide range of grain sizes are present, small grains tend to fill the spaces between larger grain so that both porosity and permeability decrease. Thus small amounts of clay or cement can clog pore throats and markedly reduce permeability without significantly reducing porosity.

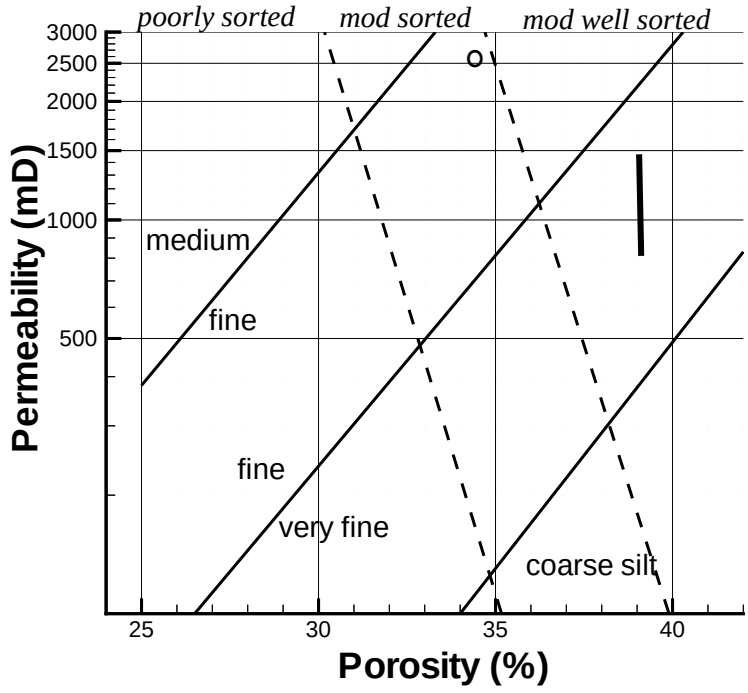

Fig.4 Porosity versus permeability for slightly to unconsolidated sands (modified from Gidman et al. 1993). The bar and open circle are estimates of porosity and permeability for the Utsira Sand.

The permeability of sands can range over 5 orders of magnitude depending on grain size, sorting and compaction. Clean, unconsolidated, coarse to medium grain sized, well sorted sands have been reported to give permeabilities in the range 10 to 150 D (Weber et al 1972). Sands that are slightly to unconsolidated and buried a few hundreds of meters show permeabilities in the range 10mD to 1D (Gidman et al 1993, Hurst 1991, 1993, Marrow et al 1969). Sandstones tend to show somewhat lower permeabilities in the mD rang, e.g. 1-20mD for turbidite sandstones in the Pyrenees (Schuppers 1993). In order to estimate the likely range of permeability and porosity in the Utsira permeability and porosity of slightly consolidated to unconsolidated sands were used as a guide. These values lie in the range of 10mD-3D for permeability and 25-40% porosity. The few measurements of permeability (800mD-3D) and porosity (35-39%) from the Utsira sand lie within this range. Gidman et al (1993) investigated the permeability and porosity of deep marine, poorly consolidated sandstones in the Inglewood Field, in the Los Angeles Basin. These consist of interbedded sandstones and mudstone (bed thickness 3 cm to 5 m) of Miocene age from a turbidite setting which may be broadly equivalent to the Utsira Sand. The lithologies ranges from massive mudstone, through interbedded mudstones and sandstones to massive sandstones. The sandstones represent a wide range of grain size and sorting. Measurements of porosity, and permeability were made on 719 core plugs giving an average porosity of 32% and a geometric mean permeability of 461mD. The data collected were also used to map out the relationship between porosity, permeability, grain size and sorting, illustrated in Fig 4. Here plots of porosity versus permeability are contoured for grain size and sorting. The contours are complex but show a tendency to form 'zones' of grain size and sorting which can act as a guide to the permeability and porosity if grain size and sorting are known (e.g. from bore hole cuttings). Plotting the permeability and porosity measurements from the core samples from the Utsira Sand indicates fine, moderately to well sorted sand which is in generally good agreement with the sample descriptions.

Permeability and porosity of clays

Permeability and porosity of clays and shales represent among the largest uncertainties in quantifying flow (Neuzil 1994). Generally permeability of clays and shales tends to be over-estimated due to the difficulty of measuring such low values close to the detection limits of instrumentation. Permeability and porosity of clays and shales are sensitive to the type of clay minerals and depth of burial. The permeability of pure clay ranges over 5 orders of magnitude. ranging from 0.1 mD (Kaolinite), to 5.0e-04 (illite) and 1.0e-06 (smectite) (Mersi and Olsen 1971) at a porosity of 50%. Porosities reduce from 80-90% to 5-10% and permeabilities reduce by up to 10 orders of magnitude for burials of up to 5 km. Generally, there is a log-linear relationship between permeability and porosity, see Fig 5 (modified from Neuzil 1994). There are a number of empirical and theoretical algorithms relating porosity, permeability, mineralogy and depth of burial for clays and shales (e.g. the Kozeny-Carmen relation, equation from England et al. 1978). However, due to the range of pore throat sizes in clays and shales permeability can easily vary by 3 orders of magnitude for the same porosity (Neuzil 1994).

The porosity and permeability of clay-silt mixtures reaches a minimum where the clay fills the pore spaces between the silt grains which are in contact with each other, generally around clay constants of 20-40% (Dewhurst and Aplin 1998, Rueil and Cathles 1999. However, it is likely that shales and clays remain permeable even at low flows with minimum permeabilities around 1.0e-06mD, and never become complete flow barriers (Neuzil 1994). Due to the plately nature of clay minerals, permeabilities of up to 3 orders of magnitude are also possible (Neuzil 1994).

The above relationships between clay mineralology, clay content and depth of burial and be used to estimate a porosity and permeability range likely for shales in the Utsira Sand and overlying Nordland shales. Data from cuttings (Lothe and Zweigel 1999) show that the average of six samples from the Nordland shales show clay contents of 52% (range 40-60%), with average clay mineral content of kaolinte (11%), mica/illite (25%), mixed layer clays (9%), chlorite (5%) and smectite (2%). The clay mineral composition is dominated by illite and kaolinite which show higher permeabilities (0.1-5e-04mD) at medium porosities (50%). A clay content of 40 to 60% is probably above to clay content needed to simply fill the pore space between the silt grains. Thus porosity and permeability will be dominated by the clay mineralogy. The pressure in the Utsira Sand is around 20MPa (at 1000m depth) which compares with three of the fields cross hatched in Fig.5 identified by Neuzil (1994). This gives a range of porosities of 10-40% and permeabilities of 0.001 to 1.0e-07mD. The equation of England (1987) relating permeability and porosity:

$$k = 4.053\phi^{8} mD$$

gives a similar range of permeabilities of 1.0e-10 to 0.003 mD for porosities of 10-40%. Thus much depends on the level of compaction of the clays in the Utsira Sand and Nordland shale for which there is presently no information. Additional information on the general trends of porosity with depth for the North Sea (Sclater and Christie 1980) may help to narrow this range.

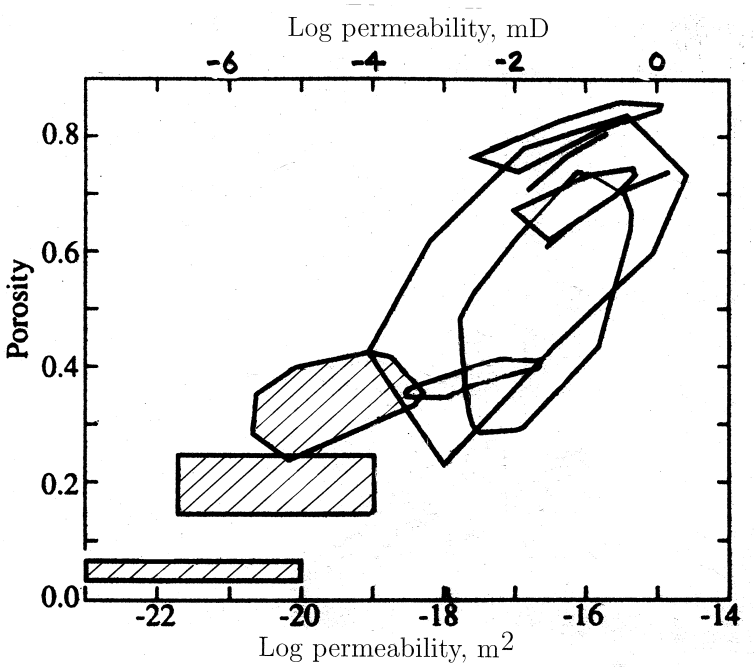

Fig.5 Permeability versus porosity for shales (modified from Neuzil 1994). The cross-hatched fields are those that have pressure conditions most closely resembling that of the Utsira Formation.

These trends (Fig.6) suggest porosities of around 40% for sandstones at 1000m depth which is in good agreement with the measured porosities from the core samples (39%). The shale trend (Fig.6) suggest porosities of around 30%. In the formula from England et al. (1978) this gives a permeability of 3.0e-04mD and on the plot of Neuzil (1994) suggests a range of possible permeabilities from 0.01 to 1.0e-06 mD.

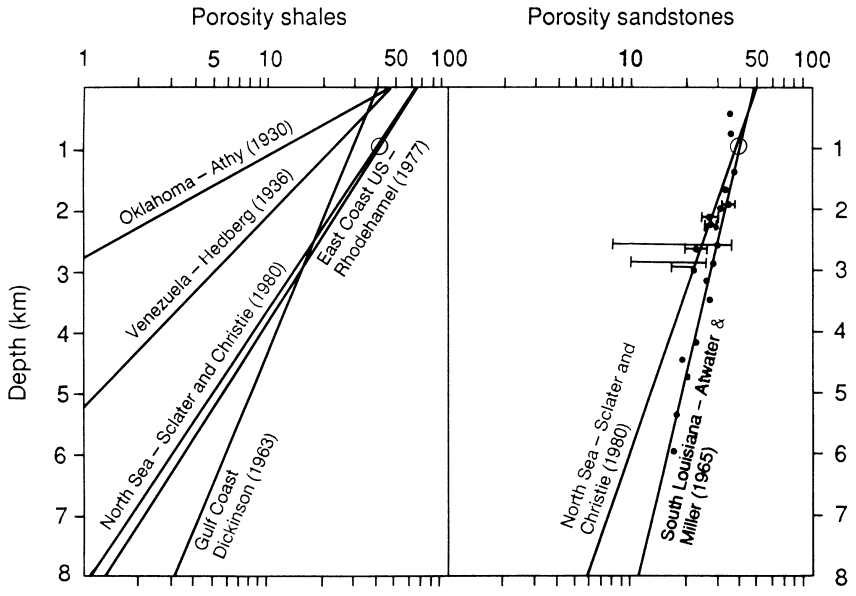

Fig.6 Trends for porosity versus depth for sands and shales (after Sclater and Christie 1980). The open circles represent the depth of the Utsira Formation at the injection point.

Modelling sedimentary architectures

Observations of rocks and sediments show that their physical properties (such as hydraulic or mechanical properties) show significant variability. Geological formations are composed of a number of distinct features such as layers of differing lithology, sedimentary structures, and tectonic structures such as fractures (joints, faults) and folds. As a result, field measurements of physical and chemical properties such as porosity and permeability show a large degree of variability. In addition, hard data on rock properties through measurements from bore holes or geophysical surveys are generally sparse and the measurement themselves often uncertain. As a result, the level of information is rarely sufficient to allow a deterministic approach to estimating flow and transport properties. It is therefore more realistic to adopt a stochastic approach where the precise geometry of any location cannot be faithfully reproduced but where realizations that posses similar spatial properties are created. In addition, properties of geological formations rarely vary in a smooth fashion but variations tend to be discrete in nature such as beds of differing lithology and occurrence of fractures.

A variety of techniques have been developed to describe geological heterogeneity. These include the kriging, spectral, perturbation, multi-variate, turning bands and nearest neighbour methods. Most of these methods require hard data in the form of measurements of properties to be simulated such as porosity and permeability. Generally, there is very sparse hard data available, but data of a soft nature may be much more readily available such as geological maps and bore hole logs which are easier and often less expensive to collect. The approach adopted here is to simulating hydraulic parameter fields such as porosity and permeability using the coupled Markov Chain method (Elfeki, Uffink and Barends 1997) which can take full advantage of 'soft' data. Other advantages are that it is simple to implement, conditional simulation is easy, and it is not computationally intensive.

The Coupled Markov Chain Model

In terms of a spatial field, a Markov chain is a probabilistic model where the state at any point is dependent only on its immediate surroundings and is independent of states further away. This model does not use variograms or autocovariance functions as most other models do, but uses conditional probabilities. Conditional probabilities have the advantage that they can be interpreted in terms of geology more easily than variograms or autocovarience functions. The state at any point is given by a 'transition probability' which specifies the probability of the state type given the states in its immediately vicinity. Transition probabilities are defined as a relative frequency of transitions from a certain state to another state in a system that is composed of a number of states. These probabilities can be arranged in matrix form:

$$\begin{bmatrix} p_{11}.p_{12}\ldots\ldots\ldots p_{1n} \\ p_{21}.p_{22}\ldots\ldots\ldots p_{2n} \\ . \\ . \\ p_{n1}.p_{n2}\ldots\ldots\ldots p_{nn} \end{bmatrix}$$

where P_{kl} is the probability of transition from state S_k to state S_l and n is the number of states in the system. Here the elements must be positive and the elements of each row must sum to 1. A coupled Markov chain describes the joint behaviour of pairs of independent systems. The coupled transition probability matrix is given by:

$P_{(ij,lk)} = P_{il} \,.\, P_{jk}$

In the case of a 2D field, these two matrices are the horizontal and the vertical transition probability matrices which define the probabilities of a change of state in the horizontal and vertical directions.

Generating a 2D field using the coupled Markov chain method

The method is illustrated below for the simple case of parallel horizontal layers. In the horizontal direction, the state is constant (no change), thus the probability that the initial state gives rise to itself is 1.0 and to any other state is zero. The horizontal transition probability matrix, for a system of 4 states, is thus:

$$\begin{bmatrix} 1.0 & 0.0 & 0.0 & 0.0 \\ 0.0 & 1.0 & 0.0 & 0.0 \\ 0.0 & 0.0 & 1.0 & 0.0 \\ 0.0 & 0.0 & 0.0 & 1.0 \end{bmatrix}$$

In the vertical direction transitions between a state and any other are equally likely and the vertical transition probability matrix is:

$$\begin{bmatrix} 0.25 & 0.25 & 0.25 & 0.25 \\ 0.25 & 0.25 & 0.25 & 0.25 \\ 0.25 & 0.25 & 0.25 & 0.25 \\ 0.25 & 0.25 & 0.25 & 0.25 \end{bmatrix}$$

A 2D field of regular cells satisfying these two transition probability matrices is generated in the following manner:

1) Generate the top row using the horizontal transition probability matrix. The first cell is assigned (randomly or deterministically) a state, *j*, and the probabilities of the state of the next cell are given by *jth* row of the horizontal transition matrix. The next state is chosen randomly, conditioned by these probabilities. Since in this case the probabilities are zero except in the case of state *j*, the row is composed of cells of the same state in all cases.

2) Generate the left hand column using the vertical transition matrix in the same manner as the top row. The vertical transition probability matrix has elements of equal value and therefore there is an equal chance of any state, including the previous one, occurring.

3) Generate the rest of the grid of cells starting at the left hand edge of row 2 and working down to the right hand cell of the bottom row. In these cells, the state of each cell depends on the states of the cell to its left and the cell above. Now the probabilities are determined by multiplying the appropriate rows of the horizontal and vertical transition probability matrices together. These products must be normalized by the sum of the products to ensure that the probabilities sum to 1. In this example, only one of the products is non-zero and so rows of same state cells are generated, determined by the first column of cells, see Fig.7(a).

In addition to horizontal layering, sloping bedding can be simulated by altering the algorithm above so that the state of a cell depends on the states of the cell to the left (horizontal transition probability matrix) and the cell to the left or right of the cell above (vertical transition probability matrix). This produces beds with slopes to the right or left. The angle of the slope depends on the cell shape and in the case of square cell produces slopes of 45^{o}. Complex nested models can also be created by superimposing models that sloping bedding on simulations of horizontal layering. In Fig.7, a variety of fields and their horizontal and vertical transition probability matrices are shown.

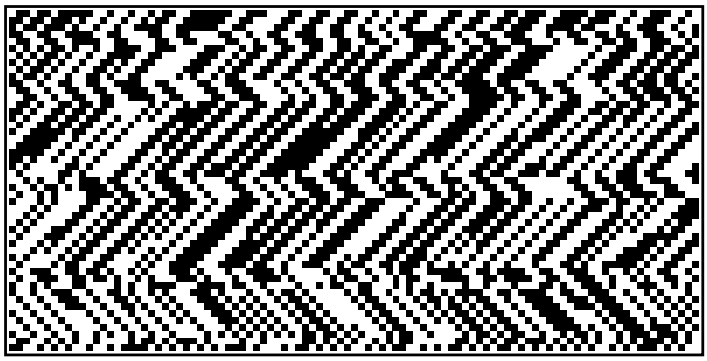

Fig.7 Examples of fields generated using the coupled Markov chain model. Top – horizontal continuous layers, middle – horizontal discontinuous layers, bottom – cross-bedding.

Generating transition probability matrices

Horizontal and vertical transition probability matrices can be generated from geological maps or sections (e.g. seismic) or well logs by the following procedure:

1)..Divide the section through the map or the bore hole log into equal sized cells, of the size required for the final model. These cells should be small enough to capture the level of detail required in the section. Assign to each division a 'state'. This could be based on, for instance, lithology, grain size, sedimentary structure type, fracture frequency, or physical properties such as permeability and porosity.

2) From the sequence of states, count the number of transitions from each state to the next for all possible combinations of states. Enter these values into a matrix and normalize each row by the sum of transitions so that the elements sum to 1. This is the transition probability matrix.

Horizontal and vertical transition probability matrices generated in this way can then be used to create any number of stochastic realizations of the sedimentary architecture that share the same spatial properties. Such realizations can form input for flow models and be used to conduct analysis of the sensitivity of the bulk rock properties (permeability, dispersion) on spatial distribution and permeability contrasts.

Generating permeability and porosity fields for input to flow models

The information available from seismic, core and well logs suggests that one of the more likely origins for the Utsira Formation is a series of sub-marine fans composed of turbidites and related sediments. The Utsira Sand is probably composed dominantly of sands with some shales and passes into more shale rich sequences on all sides, above and below (Lothe and Zweigel 1999). A possible interpretation of this unit is that it represents a sub-marine fan lobe (see Fig.3) built up by turbidity currents which formed a braided pattern over the surface of the lobe. If the Utsira Formation represents a submarine-fan, the sedimentary structures that might be found within the Utsira Sand and more widely throughout the Utsira Formation are typically turbidite sequences of graded sand beds and inter-bedded shales on the scale of 10s metres, and cross-bedding and fluid escape structures such as dish structures and fluid escape pipes, on the scale of 10s cm to 1m. Examples of

each of these structures were generated and used to create permeability and porosity fields which form input to a two-phase flow model (section x). The different sedimentary structures simulated are described below:

Turbidite sequences.

Good examples of turbidite sequences are preserved and exposed on land in a number of locations (Pickering et al 1995). One example that has been extensively studied is found in the Pyrennian Mountains near the village of Ainsa in northern Spain (Pickering et al 1995, Schuppers 1993). Here the architecture of a sequence of late to mid Eocene age turbidite-filled (sandstones and mudstones) channels is exposed in a cliff section some 600m long and 20-40m high. The sequence shows signs of multi-phase filling and is composed of two major thinning upward sequences separated by a mudstone that spans the channel. The sediments consist of normally graded sandstone beds, sandy conglomerates, intercalations of very fine-grained, thin bedded (2-6 cm) sandstones and mudstones, and mudstones (Schuppers 1993). Overall the sediments are dominated by sands but have many mudstones from 10 cm to 2 m thick inter-bedded with sands. The channel is most sand-rich near the centre where sections of sandstones with no shales up to 15 m and frequently over 2-3 m occur. The majority of mudstones layers are under 1m thick and very few are over 2 m thick. These features are consistent with the available information from the Utsira Sand, i.e. that sections of 9 m of uninterrupted sand occur (core) and that 14 shale claystone horizons thicker than around 1m occur in some in 200m of the sediments, giving a mean spacing of 14m (Lothe and Zweigel 1999, Torp 1999). This section thus provides, as far as the present state of knowledge allows, a reasonable analogue for the Utsira Sand.

Detail vertical logs with a total length of 111m of the lithologies and their grain sizes from the Ainsa section (Clark 1995) were used to generate a vertical transition probability matrix for the Ainsa sequence. For this, cells of 30 cm size were used which adequately represents most of the mudstone layers. The mudstone layers extend laterally from 600m down to around 5m and show a log-normal length distribution which is very similar to that estimated from the Frigg Field in the North Sea (Schuppers 1993). This indicates that the majority of shales are short, around the mode of about 50m or less.

In order to test the effect of shale or mudstone length on the fluid flow behaviour, three models with varying horizontal persistence of the layering were generated, see Fig.8 for examples. The generated area represents a 38 by 38 region and the minimum shale length in the simulations varies from over 40m, to around 20m and around 5m in length. Permeabilities and porosities were assigned to lithologies using the information on grain size (Clark 1995) and the relation between grain size, sorting and permeability and porosity presented in Fig.4 (adapted from Gidman et al 1993). For all lithologies, it was assumed that permeability is log-normally distributed about a mean with a spatially randomly distribution. From the literature, permeability variations of half an order of magnitude within single sedimentary beds are common (e.g. Morrow et al 1969, Hurst 1991, Hurst 1993, Schuppers 1993). To mimic this behaviour, a standard deviation of log permeability of 0.1 was used. This means that 90% of the permeability distribution will lie within a range of 0.6 of an order of magnitude. The parameters for the different lithologies are listed in Table 1:

Table 1 - lithology classes for the Ainsa turbidite sequence and associated permeability and porosity.

Lithology	Permeability (D)	Standard dev. log K	Porosity
shale/clay	0.00005	0.1	0.3
very fine sand	0.01	0.1	0.32
fine sand	0.4	0.1	0.37
medium sand	0.2	0.1	0.27
coarse sand	0.2	0.1	0.27

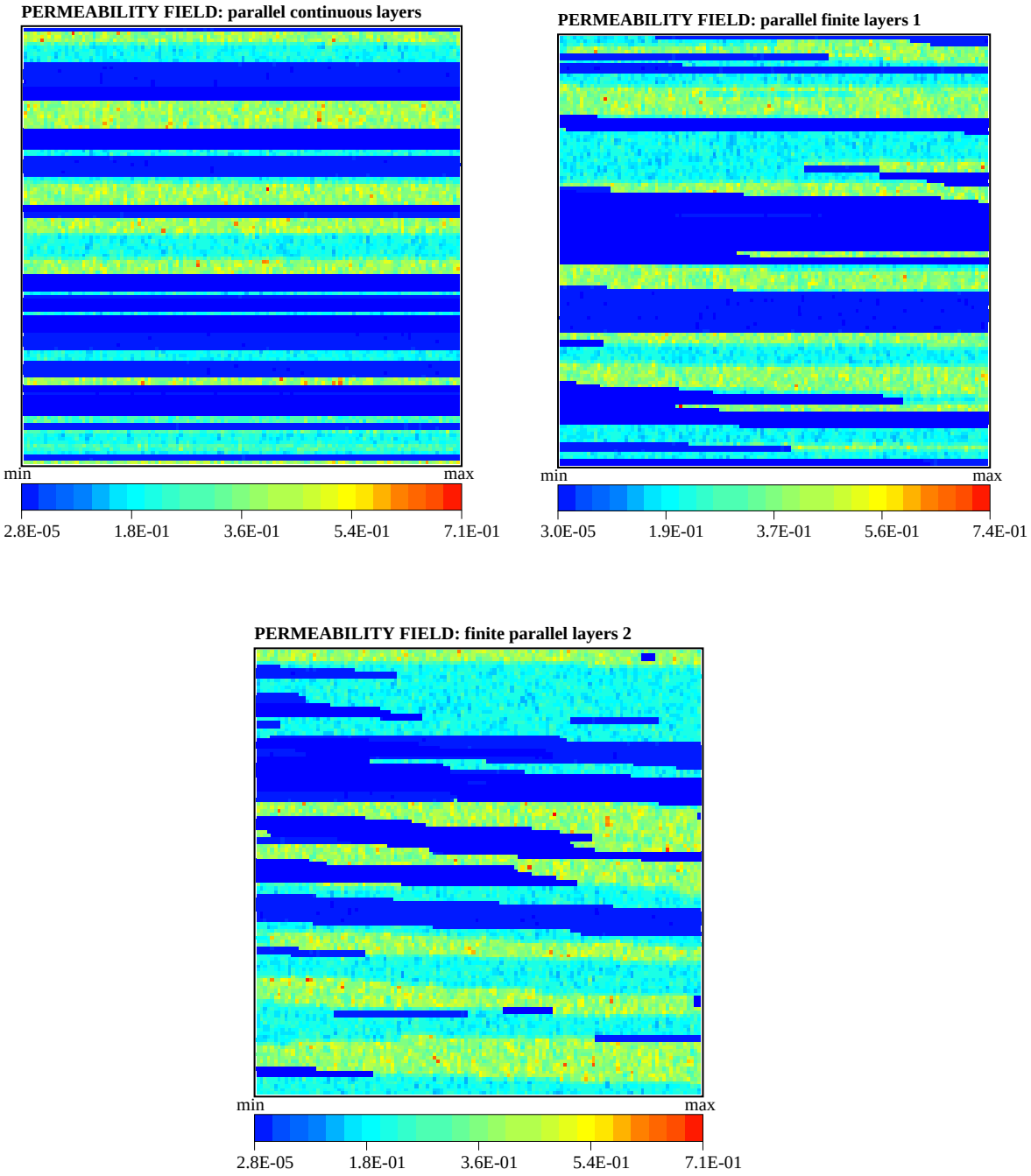

Fig.8 Permeability fields for examples of turbidite sequences representing an area of 38 by 38m. Top left – parallel continuous layers, top right – discontinuous layers (shales around 40m), bottom - discontinuous layers (shales around 5m).

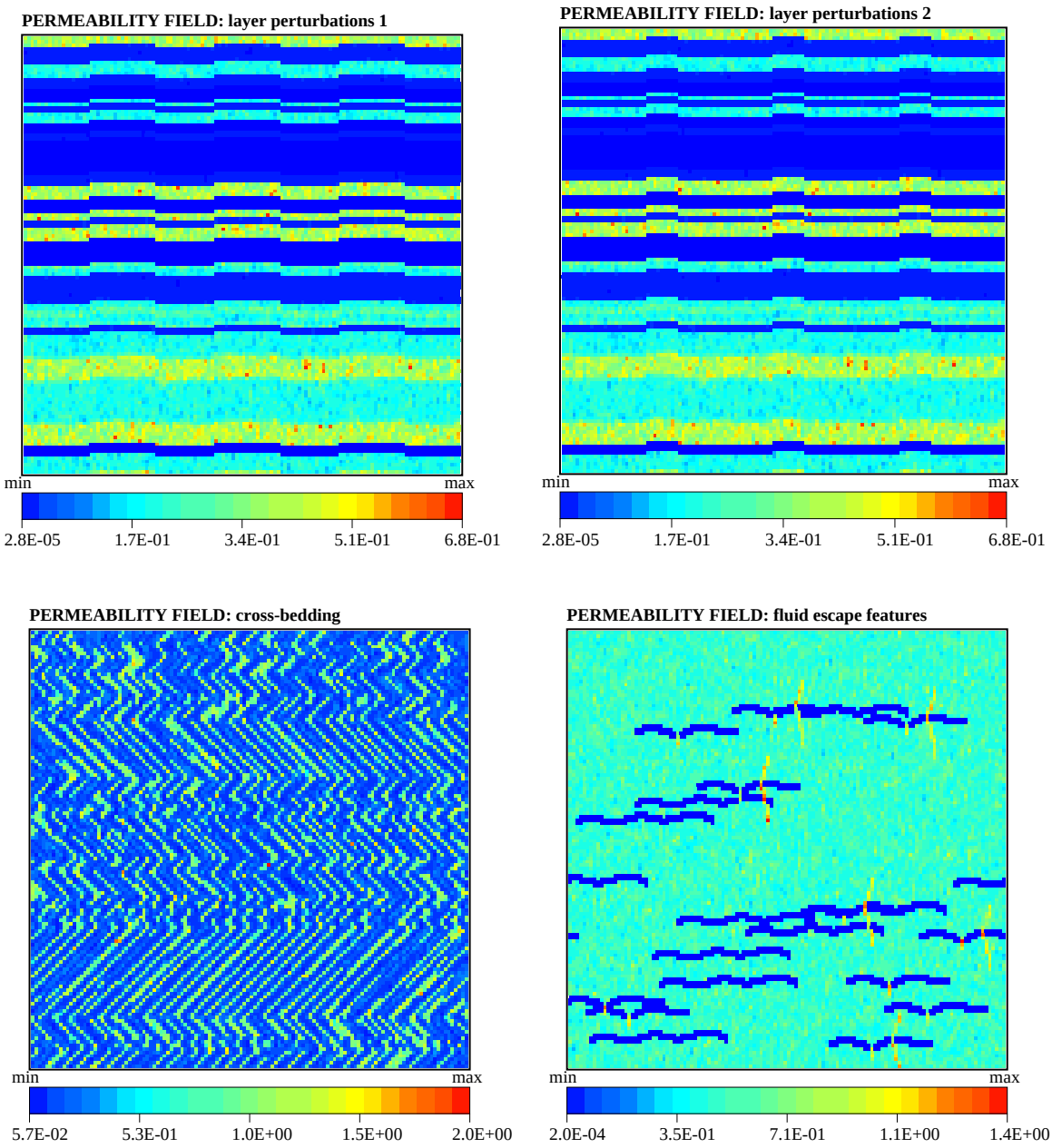

Fig.8 (cont.) Permeability fields for:, top left – parallel continuous layers with wave like perturbations 1, top right – parallel continuous layers with wave like perturbations 2 (38 by 38m), bottom left – cross-bedding (0.5 by 0.5m) and bottom right – massive sands with fluid escape structures (0.6 by 0.6m).

Another possible deviation from horizontal parallel layering could be caused by minor folding. Such folding may occur due to differential compaction around mud volcanoes at the base of the Utsira Formation (Lothe and Zweigel 1999) or around faults. To test the effect of small perturbation in the geometry of the layering, two sinusoidal waves of small amplitude (1 cell and 3 cells) were imposed on the layering, see Fig.8.

Cross-bedding

Cross-bedding on a variety of scales is a common feature of sandstones of all environments. In turbidites, ripple cross laminations are common in division C (sandstone) of the classic turbidite Bouma sequence that might be expected on supra-fan lobes and basin parts of the fan, and in coarse grain and pebbly sandstones expected in the middle (supra-fan lobes) to upper fan areas . The sets are commonly 5 to 10 cm thick with trough or planar cross bedding. Each cross beds consists of graded unit with coarser material at the base and finer material at the top. This can generate permeability differences by commonly a factor of three and up to 1 order of magnitude (Weber et al 1972, Pickup et al 1996).

In order to simulate successive cross laminated beds using the coupled Markov chain model, a simulation was first made of horizontal beds of varying thickness and then each bed was superimposed by a sloping cross lamination pattern using two states. These two states were given permeabilities representative of fine sand and medium grained sand (Fig.4), see Table 2. A contrast of 1 order of magnitude was chosen to represent the maximum possible effect on fluid flow. An example of a simulated permeability field is shown in Fig.8.

Table 2: lithologies and parameters for cross-bedding simulations

Lithology	permeability (D)	standard dev. log K	porosity
fine sand	0.1	0.1	0.3
medium sand	1.0	0.1	0.35

Fluid escape structures

Massive sandstones found within marine fan sequences often contain fluid escape features. These sandstones are generally deposited rapidly from a sediment loaded turbidity current within which sediment is kept in suspension by turbulent flow. On deposition, the sediment grains settle under gravity and large quantities of fluid must escape to allow the sediment to stabilize. The process of water expulsion gives rise to fluid escape structures. These include dish structures, thin horizontal layers (less than 1 mm thick) of fine grain sediment with spoon-shaped geometries, and fluid escape pipes, vertical pipe-like structures of clean sand. The dish structures represent potential flow barriers while the fluid escape pipes have enhanced permeability because the fine sediment has been washed out. Dish structures and fluid escape pipes often occur together and fluid escape pipes sometimes occur where two upturned edges of dish structures meet forming a channel for fluid flow. Dish structures are commonly 10 cm long and can occurs in strings. Fluid escape pipes are commonly 10 cm long and around 1 cm wide.

Table 3: lithologies and parameters for massive sandstone with fluid escape structures

Lithology	permeability (D)	standard dev. log K	porosity
dish structure	0.0002	0.0	0.30
fluid escape pipe	1.00	0.1	0.37
massive sands	0.5	0.1	0.32

A simulation of massive sandstones with dish structures and fluid escape pipes was generated using a 'template' method. Three templates were constructed for (a) dish structures alone, (b) dish structures with fluid escape pipes and (c) fluid escape pipes alone. These three templates were then placed randomly in a homogeneous field representing massive sandstones. The cells representing massive sandstone, dish structure and fluid escape pipe were assigned permeabilities and porosities listed in Table 3. An example of the permeability field for these simulations, representing an area of 63 by 63 cm, is shown in Fig.8.

The above simulations of sedimentary architecture on a variety of scales were used to generate a total of seven permeability and porosity field types. Ten realizations of each field type were generated and these fields were used as input to the two phase flow model described in the next section to test the sensitivity of the flow properties to variations in sedimentary architecture.

Two-phase flow in heterogeneous sediments

The presence of heterogeneities in permeable sediments results in highly heterogeneous permeability fields which have a large impact on the relative flow of two immiscible fluids. This results in 'viscous fingering' (e.g. Feder 1989) which generates complex fluid fronts and highly variable fluid saturation fields. Such phenomena make prediction of the migration rates and dispersion of injected fluid behaviour difficult. This phenomenon has been intensively studied for the case of oil and water where such effects make efficient recovery from petroleum reservoirs difficult and complex (e.g. Barker and Thibeau 1997, Kyte and Berry 1975, Langlo 1992, Pickup et al 1994). In the case of injected supercritical CO_2, the fluids have different densities (CO_2 is slightly less dense than water), but also different viscosities with about an order of magnitude difference between CO_2 and water. Supercritical CO_2 is soluble in water but the dissolution takes place very slowly so that on a time scale of hours to months advection effects dominate and supercritical CO_2 and water can be treated as two immiscible fluids. The extreme viscosity ratio (of the order 1:10) results is a more smeared out fluid front and more extreme fingering effects due to sediment heterogeneities than is normally the case for water and oil.

Relative permeability and fluid fronts

When the two immiscible phases occupy the rock pore space, the space through which each phase can flow depends on the saturation (Pettersen 1990). Thus the relative permeability of each phase depends on the absolute permeability of the rock and the saturation (or concentration) of that phase. The simultaneous flow of the two fluid phases through a rock mass can be described by the two phase version of Darcy's law:

$$U_1 = \frac{K_{r1}}{12\mu_1}\Delta P_1 \quad (1) \quad \text{and} \quad U_2 = \frac{K_{r2}}{12\mu_2}\Delta P_2 \quad (2)$$

where K_{r1} and K_{r2} are the relative permeabilities, μ_1 and μ_2 are the viscosities and ΔP_1 and ΔP_2 are the pressure gradients in the fluid phases 1 and 2.

When two phases occupy the pore space, one fluid is wetting and the other non-wetting. In a rock with oil and water, water is normally the wetting phase. The wetting phase has the greater affinity for the rock surface and forms a thin film around the rock grains. Due to friction between the wetting fluid and the rock grains, this film of fluid will always remain and gives rise to an irreducible water saturation, S_{wc}. In addition, due to the complex geometry of the pore space, small pockets of the non-wetting phase become trapped and form an irreducible fraction, S_{cr}. Thus under flow the saturation of the two phases vary between these two values. There is no information available about the relative wetting properties of water and supercritical CO_2. However, since the pore space is water filled before CO_2 injection it is assumed that the rock is water wet.

Fluids with intermediate values of saturation travel faster than fluids with low saturations. In the case of water injection, this means that intermediate water saturations try to 'overtake' the lower saturations resulting in the formation of a saturation discontinuity or a 'shock' front. This phenomenon acts to maintain a sharp contact between the two fluids at which there are very abrupt changes in saturation. The shock saturation is independent of time.

The relative permeabilities in equations 1 and 2 vary between 0 and 1 and depend on the saturation of the fluids in the rock. At irreducible water saturation, S_{wc}, water will not flow and $K_{rw}=0$, while at residual saturation, S_{cr}, CO_2 will not flow and $K_{rc}=0$. Between these values, relative permeabilities can take on different values depending on the properties of the rock, but generally such that their sum is less than 1. For rock matrix, relative permeability curves are generally determined from rock samples in the laboratory. For the case of water and oil they show the typical form shown in Fig.9. However, there is at present no information on what rock relative permeability curves look like for supercritical CO_2 and water, so the simple curves illustrated in Fig.9 are used.

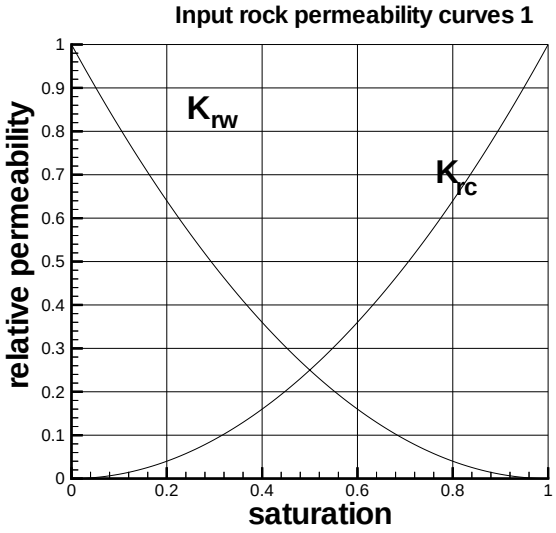

Fig.9 Assumed simple rock relative permeability curves for water (K_{rw}) and supercritical CO_2 (K_{rc}).

Pseudo functions for rock volumes

Relative permeability curves from laboratory experiments on rock samples some cm in size are only valid for larger volumes as long as the rock remains homogeneous. Generally this is not the case, and heterogeneities such as sedimentary structure and fractures significantly modify the behaviour of two phase flow. Thus for describing two phase flow in the average simulator grid block which is of the order of 100's metres, 'pseudo' relative permeability curves must be determined.

A number of methods exist for determining pseudo curves for oil and water in petroleum reservoirs and a summary is given by Barker and Thibeau (1996). Most widely used is the method by Kyte and Berry (1975). Here fine grid simulations which can resolve the fine details of the heterogeneous permeability field are used to determine the time dependent average saturation of the block and flow rates of oil and water out of the block. These values are substituted into the two phase Darcy equations (equations 1 and 2) to give the relative permeabilities of oil and water for each average saturation. Other methods (non-dynamic) include calculating weighted averages (e.g. by transmissibility) of fine grid relative permeabilities, and the total mobility method. No method is, however, always reliable and the applicability of the results is dependent on boundary conditions of the grid block *in situ.*

To date, there exists little information in the literature on pseudo functions for different kinds of geological heterogeneity. Pickup et al (1994) have built a 'geopseudo atlas', in which geological models of fine scale sedimentary structure can be built, or selected from templates, and bulk permeabilities and pseudo relative permeability curves determined. To date, however, there exists no information on pseudos for the flow of supercritical CO_2 and water in heterogeneous sediments. Some large scale simulators, such as Eclipse, contain routines for calculating pseudo curves. The

reliability of the results are, however, dependent on the ability of the simulator to cope with high permeability contrasts. In addition, the capability of the simulator to simulate the details of the sediment architecture is often limited.

In this project, a two phase flow program (written at the Department of Applied Mathematics, University of Bergen, Langlo 1992), specifically designed to handle large permeability contrasts and reproduce accurately the complexity of saturation front, has been used to determine pseudo functions for different sediment heterogeneities. The pseudo curves determined from these patterns can be used a first guide to pseudo functions for supercritical CO_2 and water in the heterogeneous sediments that might occur in the Utsira Formation.

A two phase flow model for heterogeneous sediments

Sediment heterogeneities can represent permeability differences of several orders of magnitude and therefore made high demands on the numerical methods used. The model must also be able to handle large discontinuities in the permeability field that result from the presence of e.g. shale layers adjacent to high permeability sands and to resolve sharp and geometrically complex fluid fronts. At the Institute of Applied Mathematics in Bergen University much expertise in the numerical modeling of two phase flow in heterogeneous porous media has been carried out through the group of Prof. Magne Espedal. The chosen model was developed by Peder Langlo and was originally designed to simulate two phase flow in heterogeneous porous media (Langlo 1992).

The model

The pressure equation is solved by a finite element method, where Multigrid is used as a solver. The velocity, u_x, is determined from the pressure by a central difference method:

$$u_x = KM(p(i+1, j) - p(i-1, j)) / 2dx$$

where K is the permeability, M is a mobility function which contains the relative permeabilities and $p(i,j)$ is the pressure at the *ith* and *jth* node.

The saturation equation is solved by an operator splitting method where the hyperbolic part of the equation is solved by integrating backwards along the characteristics to determine a approximate solution on the new time level.

The remaining elliptic part of the saturation equation is solved by a finite element method, with a conjugate gradient solver on sub-domains in the vicinity of the saturation front. However it was found that the model, as it is today, could not handle Dirichlet boundary conditions at the outlet and thus the model was run without this part. This means that capillary forces are neglected. In an oil recovery situation this does not create great errors, because the saturation equation is dominated by the convective/hyperbolic part of the equation. However, there may be effects which the model in its present state will not capture. The main weakness of the model is the way that velocity is derived from the pressure by a central difference scheme, because it can not guarantee that the mass is conserved to a high degree of accuracy. There are other codes that handle the mass balance

better, such as Eclipse, but these models tend to smooth the velocity field and do not capture the full effects of the heterogeneous permeability field.

Model input

Input to the model consists of permeability and porosity fields, local (core scale) relative permeability curves, fluid viscosities, flow rates at left and right boundaries, number of time steps and time step size.

Permeability and porosity fields

Permeability and porosity fields were determined using the coupled Markov chain simulation model and other simulation methods described in the previous section, generating field of 128 by 128 cells. From these, the permeability governing the flow of fluid from each cell to its neighbour above and to the right are calculated from the harmonic average of the two cell permeabilities. These vertical and horizontal permeability fields of 127 by 127 cells are used as input to the model.

Viscosity of water and supercritical CO_2

The reservoir conditions at a depth of 987m are a pore fluid pressure of 10MPa and temperature of 37^oC (Torp 1999). At atmospheric pressures, CO_2 becomes liquid at 37^oC . In the system H_2O-CO_2, the invariant point where liquid and gaseous CO_2 phases and water coexist is at around 10^oC and 4.5 MPa (Wadsley 1993). For temperatures above 10-15^oC, the possible combinations are liquid CO_2 and liquid H2O at higher pressures (above 5-10 MPa) and gaseous CO_2 and liquid water at lower pressures. The reservoir conditions (37^oC, 10MPa) lie close to the boundary of these two states but it is thought that CO_2 exists primarily as a liquid at these depths (Torp 1999). The two phase flow model is only valid for two immiscible liquids and thus can only simulate the behaviour of supercritical CO_2 and water. The viscosities of water and liquid CO_2 at the depth and temperature of the reservoir can be estimated from the available data given in Table 1. These values of the viscosity of liquid CO_2 compare with the viscosity of gaseous CO_2 of 0.014 mPa s. These data give a viscosity ratio for CO_2: water of around 15:1 for pure CO_2 and water in the temperature range 20-40^oC. However, the formation waters in the Utsira Sand are saline with salinities probably similar to that at Oseberg 200 km to the north of 33g/l (Torp 1999). This is slightly less saline than sea water (35g/l). In addition the CO_2 injected contains some 2-3% methane the effect of which on viscosity is unknown. For the purposes of simulation a conservative estimate of the viscosity ratio of 1 order of magnitude (10:1) was used. This viscosity ratio is much higher than is commonly the case for oil and water (around 1:2 for water:oil).

Table 1: data on viscosity of water and liquid CO_2 (James and Lord 1992).

T (^oC)	Viscosity of water at 49 MPa, (mPa s)	T (^oC)	Viscosity of supercritical CO_2 (MPa)
20	0.992	-50	0.227
30	0.796	0	0.089
50	0.339	30	0.053

Relative permeability curves for water - liquid CO_2

No data is presently available for rock relative permeability curves for liquid CO_2 and water. Thus for the simulations simple symmetrical, convex curves (Fig.9) were used for all lithologies. This implies some influence of capillary forces at the pore scale. However user defined relative permeability curves can be input to the model, so there is the possibility of modifying them when more information is available.

Model boundary conditions

The top and bottom boundaries of the model are set to no flow and, at the first time step, constant flow rates are set along the left and right hand boundaries. Using the permeability field and the input flow rates the pressure field is determined and this pressure difference across the model maintain thorough the run. The pressure field internal to the model is recalculated at every time step. At the start of simulations, the supercritical CO_2 saturation is set to 1 at the left boundary and decreases linearly to the shock saturation in 0.2 times the model size. The model was run for 100 to 200 time steps for which the saturation, pressure and velocity fields were determined. The model was run on the Cray Origin 2000 at the University of Bergen (ParaLab). Runs of 200 time steps take about 10 to 15 minutes of run time.

Model Output

The model outputs the pressure, velocity and saturation fields at user specified time intervals. These consist of values are every node in the 127 by 127 grid. In order to save space, saturation fields are output at user specified time intervals, while the saturation at the outflow boundary are output at every time step. A series of graphic programs have been created to present the model results. 'Snapshots' of the saturation field at specific time intervals can be produced. A flow evolution plot is created which shows the changes in saturation along the outflow boundary with time. These saturation are summed to show the total saturation at the outflow boundary with time.

From the output of the flow model, the relative permeabilities for the whole region at each time step are calculated using the method by Kyte and Berry (1975). The flows of water and oil at the

outflow boundary are determined from the column of cells at the right hand side of the model. The relative permeabilities of these cells are determined from their saturation and the input rock relative permeability curves. These relative permeabilities are used with the pressure difference across each cell and the intrinsic permeability to determine the flows of water and oil through these cells. Pseudo relative permeabilities for the whole model are then calculated from the sum of these flows using the following formula:

$$k_{ri} = \sum \frac{q(i)\mu}{\Delta P k_g}$$

where *i* is supercritical CO_2 and water. Finally, for each time step the average saturation of the whole model is calculated. The values of pseudo relative permeabilities are plotted against the average saturation for the whole model at each time step to give pseudo relative permeability curves for the modelled region.

Numerical Model Results

The seven cases of permeability-porosity fields generated to represent various kinds of sediment heterogeneity have been used as input to the two phase flow model. These comprise

1) Three cases turbidite sequences with layering of varying continuity representing shale layers i) continuous ii) around 40 m and iii) around 5 m Each model represents an area of 38 by 38 m.

2) Two cases of turbidite sequences with wave like perturbations Each model represents an area of 38 by 38 m.

3) Cross-bedded sandstones. Each model represents an area of 0.5 by 0.5 m.

4) Massive sandstones with fluid escape features (dish structures and fluid escape pipes). Each model represents an area of 0.6 by 0.6 m.

These models of sediment heterogeneity were used to conduct the following numerical experiments:

1) Using a single phase flow model, the bulk rock permeability for each model was determined.

2) Series of snapshots were created to give a picture of the migration of injected CO2.

3) A sensitivity analysis was made for pseudo relative permeability curves and saturation variation with injected fluid volume using multiple realizations of the permeability and porosity fields.

Bulk Rock Permeability

A single phase flow model (Odling and Webman 1991) was used to estimate the bulk permeability of the 7 cases above. The single phase flow model was run with Dirichlet boundary conditions (constant pressure) on two opposing boundaries and no flow conditions were imposed on the other boundaries. The global permeability of the entire area was calculated from Darcy's Law for single phase flow using the flow at the right hand model boundary. Ten estimates of global permeability in two perpendicular directions (parallel and perpendicular to layering) were made using 10 realizations of each case. These give accurate estimates of global permeability in the direction of the flow. In addition, for each realization the geometric mean (arithmetic mean of log permeability) of the all cell permeabilities was calculated. This is a method sometimes used to up-scale the permeability of a complex field, since it is computationally less intensive and therefore much quicker than direct flow modelling.

In Fig.10, the global permeabilities from the flow model are plotted against the geometric means of permeability. The true global permeabilities (estimated by the flow model) cover a range of 3 orders of magnitude, slightly less than the permeabilities range within each realization (up to 4 orders of magnitude). The geometric mean permeability is, of course, constant regardless of the orientation of flow. This results in differences between the geometric means and the flow model global permeabilities. For the cases of matrix only, cross-bedding and fluid escape structures there is little difference in global permeability parallel and perpendicular to the layering, and the geometric average gives a good estimate of global permeability. In all these cases,

layering (bedding) does not present large contrasts in permeability. In the case of fluid escape structures, although thin layers of low permeability are present they are thin and discontinuous and thus produce only small effects on global permeability anisotropy.

However, where the layering displays frequent, large changes in permeability, there are large differences between global permeabilities parallel and perpendicular to bedding. This is shown by all the cases of turbidite sequences. For flow parallel to layering the high permeability layering dominates but for flow perpendicular to layering the low permeability layers dominate. Thus the geometric average, which is independent of orientation, underestimates global permeability parallel to layering and overestimated global permeability perpendicular to layering. These errors are 1-2 orders of magnitude and therefore significant and most pronounced for the direction perpendicular to layering. Global permeabilities parallel to layering for all turbidite models is similar regardless of layer continuity, but for the direction perpendicular to layering the difference between the flow model and geometric global permeabilities is greatest for continuous layering. In this case, flow is forced to go through the low permeability layers reducing global permeability.

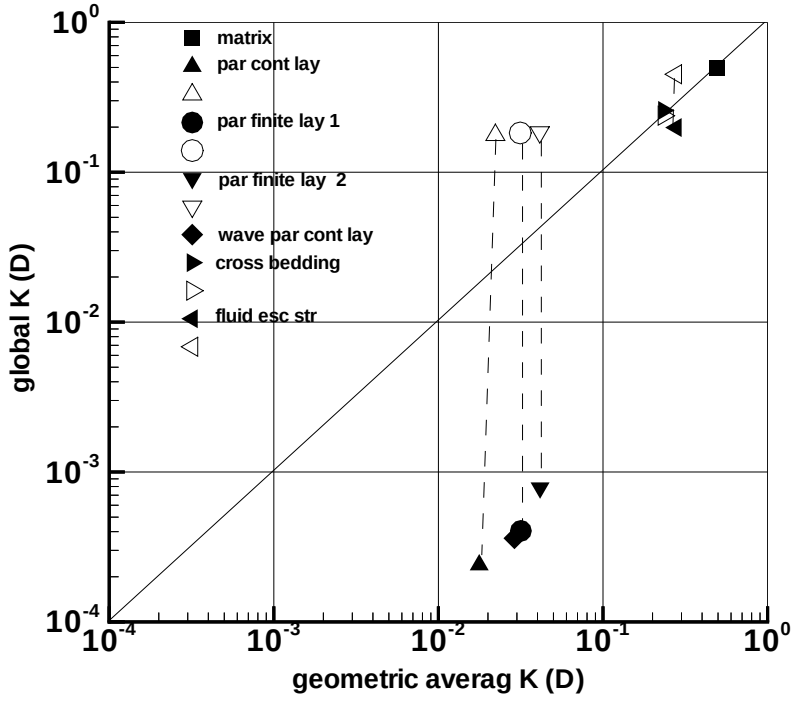

Fig.10 Global permeability determined using the flow model versus geometric mean permeability for the seven cases of sedimentary heterogeneity.

The results show that, for the cases where the layering does not represent large contrasts in permeability, the geometric mean of the permeability field gives a reasonable estimate of the global permeability. However, in the case where there is marked permeability layering, the geometric mean of the permeability field strongly overestimates global permeability perpendicular, and underestimates global permeability parallel, to layering.

Saturation field evolution

For each of the cases, a single realization was used to create a series of 6 snapshots to visualize the evolution of the flow field and CO_2 distribution. This was done using 'edge' injection (inflow along one side of the model).

The case of matrix only (Fig.11(a)) shows a simple picture of the CO_2-water front moving as a line parallel to the injection edge across the modelled area. The random variations in permeability of one half order of magnitude cause small scale fingering that is most evident in the last snapshot. Due to the high viscosity ratio, the front is highly smeared out with most of the model in the last snapshot having saturation of less then 0.5.

The case of continuous parallel turbidite layers (Fig.11(b)) shows a very similar picture to the matrix only case. This is because the layering is perfectly parallel, perpendicular to the pressure gradient. However, for the two cases of discontinuous layering (Fig.11(c) and (d)) there are marked changes with highly complex saturation fields developing as the injected CO_2 flows round the low permeability shale layers. This produces large contrasts in saturation with areas of trapped water where flow rates are very slow and thin tongues of CO_2 reaching out into the water saturated region.

The two cases of perturbed layering (Figs.11(e) and (f)) show that even small deviations from perfectly planar and parallel layering have significant effects on the flow patterns. The 'high' points or anticlines in the perturbations are places of preferential flow and the 'corners' where there are steps in the layering give rise to secondary tongues of increase CO_2 saturation. These effects increase as the CO_2 front moves through the model area being magnified at each low permeability layer crossed. The geometry of the perturbations is reflected in the frequency and the spacing of the CO_2 tongues as is seen by comparing the two examples.

The case of cross-bedding (Fig.11(g)) is similar to the case of matrix only in that the CO_2 front advances as an approximately straight line perpendicular to the pressure gradient. However, the fingering effects are enhanced compared to the matrix only case. The effect of the different directions of cross-beds is seen in the thick bed near the base of the model but these effects appear to average out over the rest of the model to produce fingering parallel to the pressure gradient.

The case of fluid escape structures (Fig.11(h)) show the most complex saturation field of all the models. The thin dish structures act as discontinuous flow barriers so this case resembles, in part, the discontinuous turbidite sequence case but with shorter low permeability layers. The fluid escape pipes form pathways of high flow which generated small CO_2 plumes at their low pressure ends. As CO_2 flows round the dish structures and along the fluid escape pipes, it leaves areas of high water saturation trapped behind the front creating highly complex and variable saturation fields.

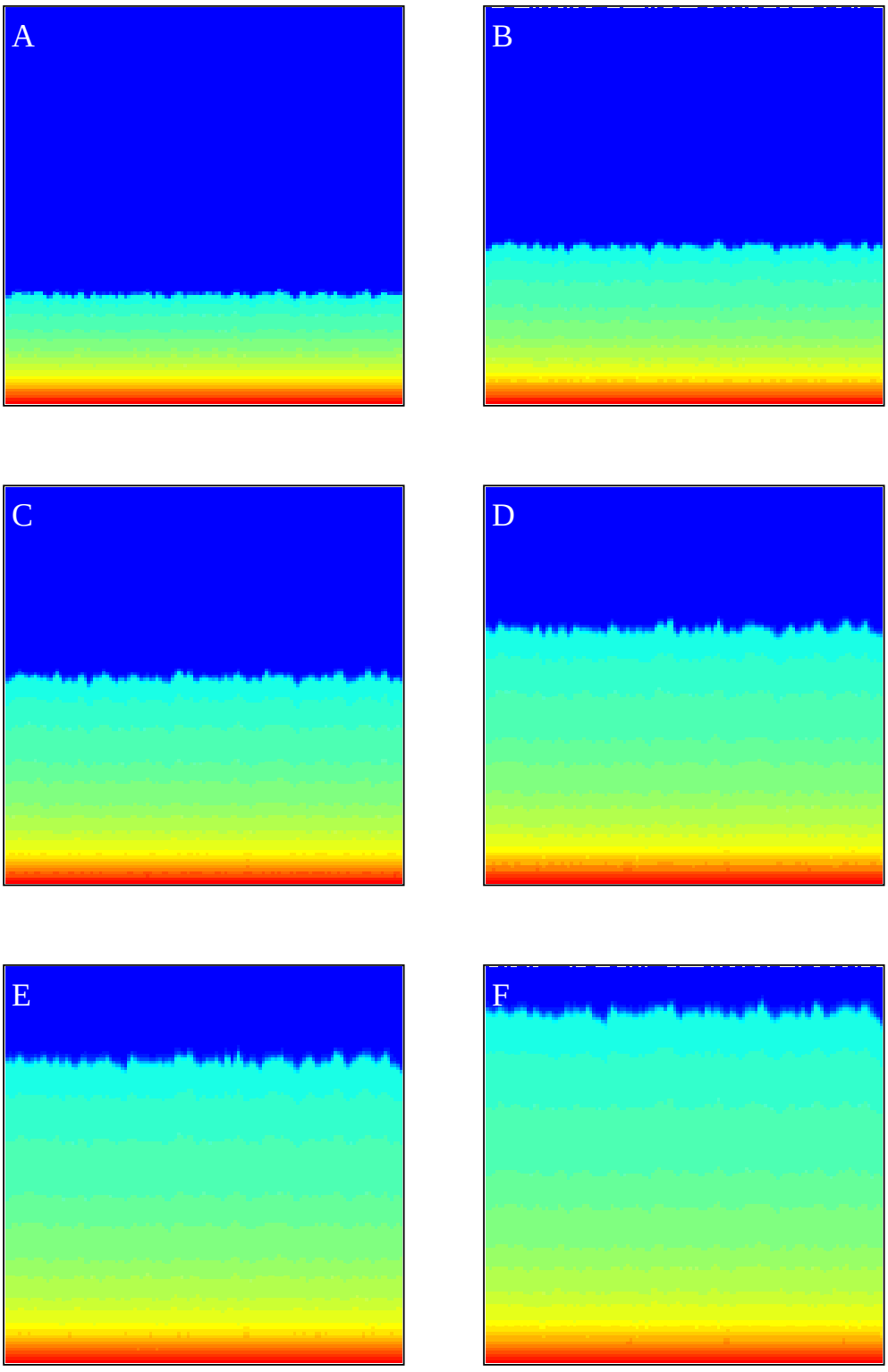

Fig.11(a) Snapshots of supercritical CO_2 and water flow in a region of homogeneous sands. The sand has a permeability of 0.1D and a standard deviation of log K of 0.1. CO_2 is injected along the bottom edge of the model which is initially water saturated. The modelled region is 38 by 38m. Boundary conditions are constant flow top and bottom and no flow conditions imposed right and left.

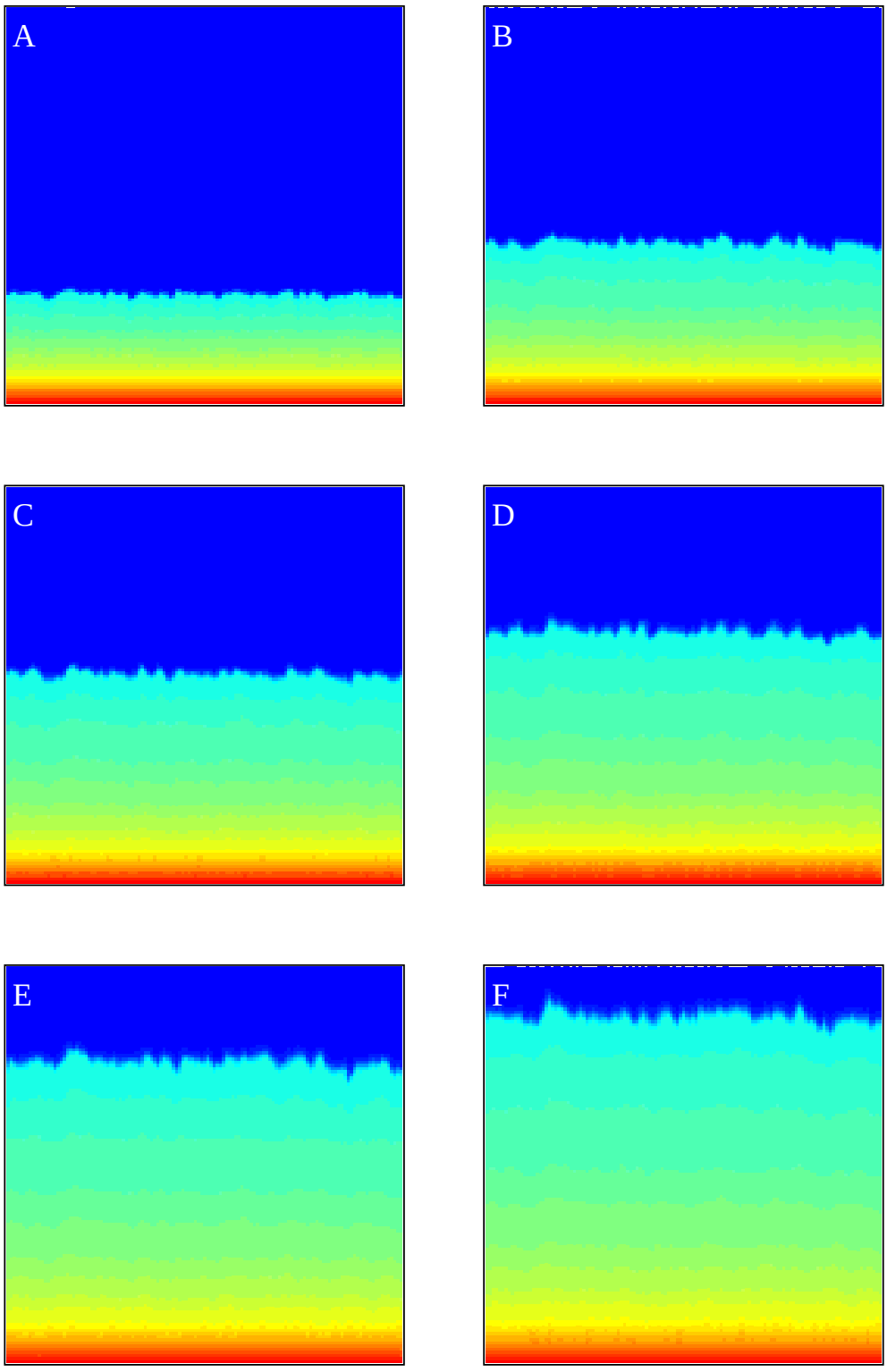

Fig.11(b) Snapshots of supercritical CO_2 and water flow in a region of turbidite beds with parallel, continuous layering. CO2 is injected along the bottom edge of the model which initially water saturated. The modelled region is 38 by 38m. Constant flow boundary conditions with flow from bottom to top and no flow conditions imposed right and left. The saturation pattern resembles that of homogeneous sandstone.

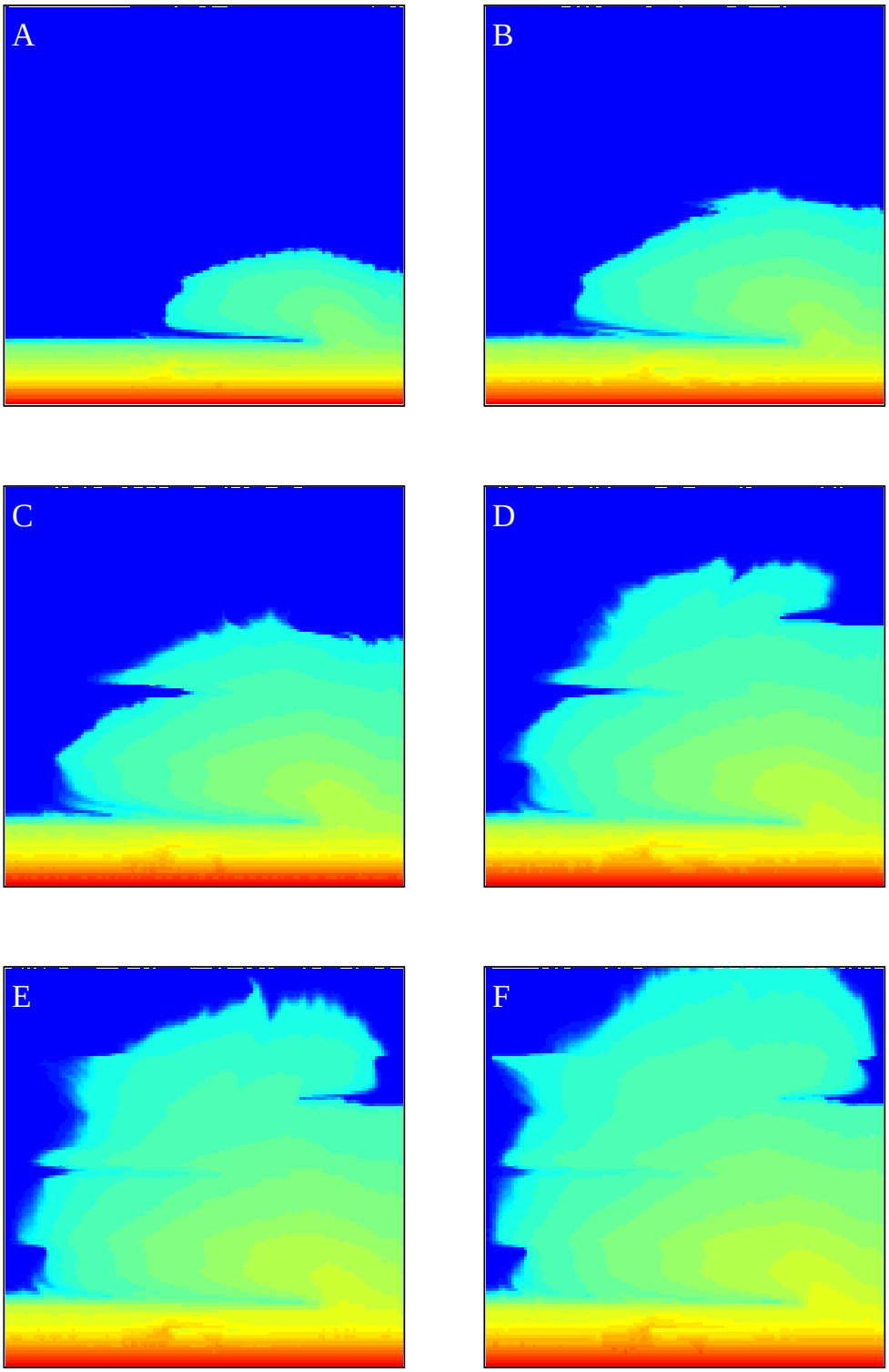

Fig.11(c) Snapshots of supercritical CO_2 and water flow in a region of turbidite beds with parallel, discontinuous layering, with shale layers around 40m long. The modelled region is 38 by 38m. CO_2 is injected along the bottom edge of the model which is initially water saturated. Constant flow boundary conditions with flow from bottom to top and no flow conditions imposed right and left. The saturation field is heterogeneous.

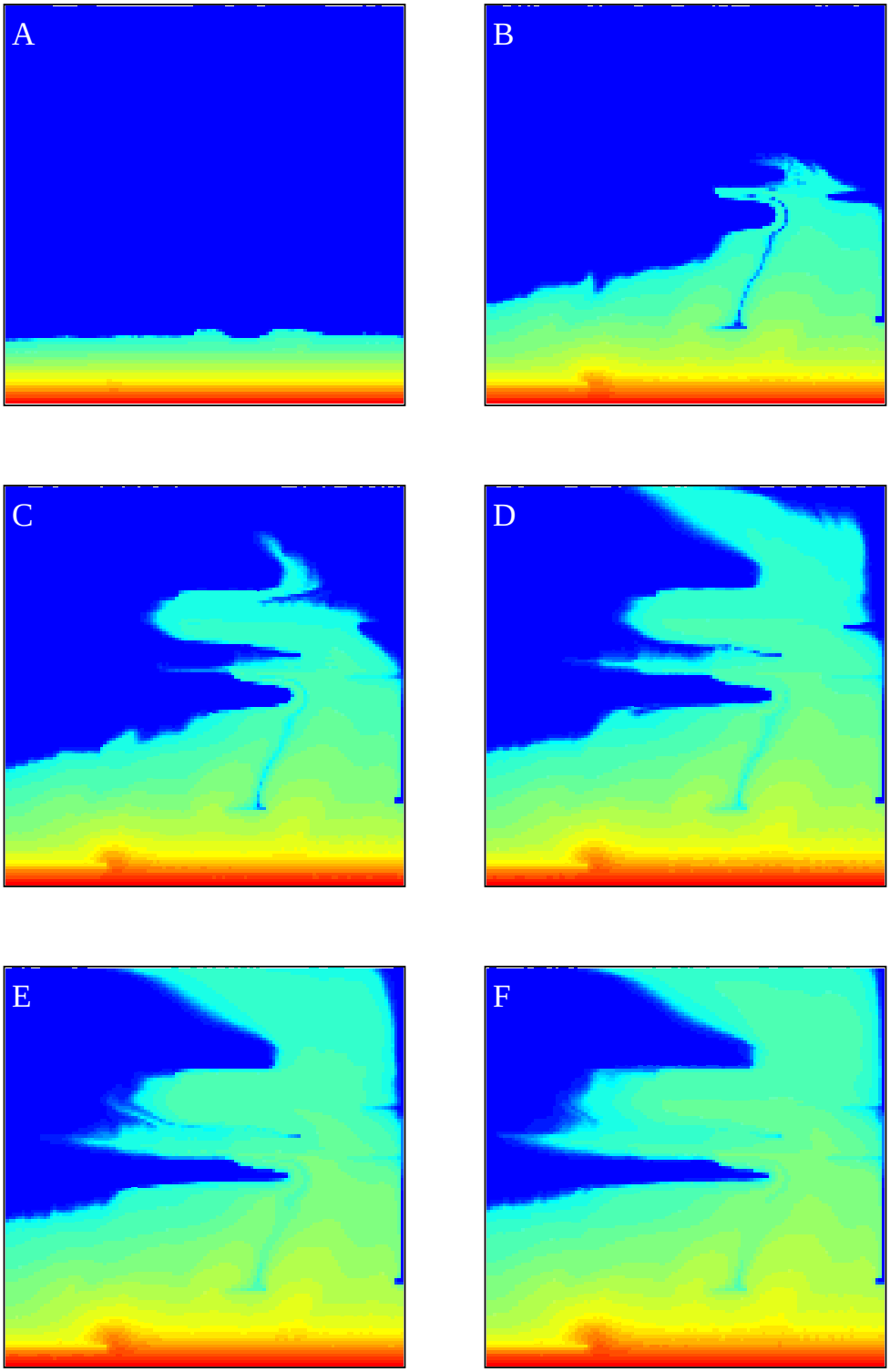

Fig.11(d) Snapshots of supercritical CO_2 and water flow in a region of turbidite beds with parallel, discontinuous layering, with shale layers around 5m long. The modelled region is 38 by 38m. CO_2 is injected along the bottom edge of the model which is initially water saturated. Constant flow boundary conditions with flow from bottom to top and no flow conditions imposed right and left. The saturation field is highly heterogeneous

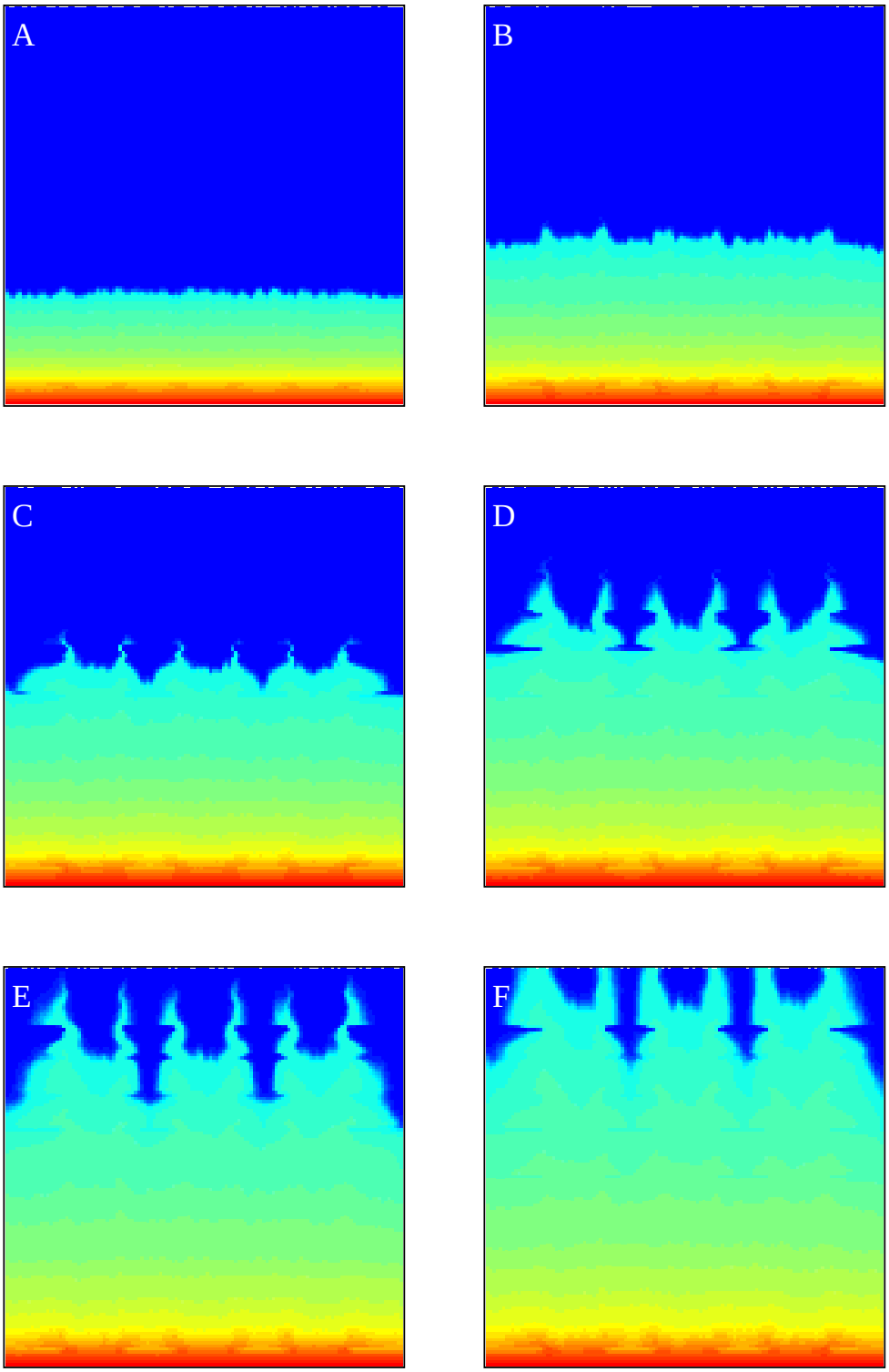

Fig.11(e) Snapshots of supercritical CO_2 and water flow in a region of turbidite beds with parallel, discontinuous layering and wave-like perturbations 1. The modelled region is 38 by 38m. CO_2 is injected along the bottom edge of the model which is initially water saturated. Constant flow boundary conditions with flow from bottom to top and no flow conditions imposed right and left. Tongues of high CO_2 saturation develop corresponding to anticlines in the layering.

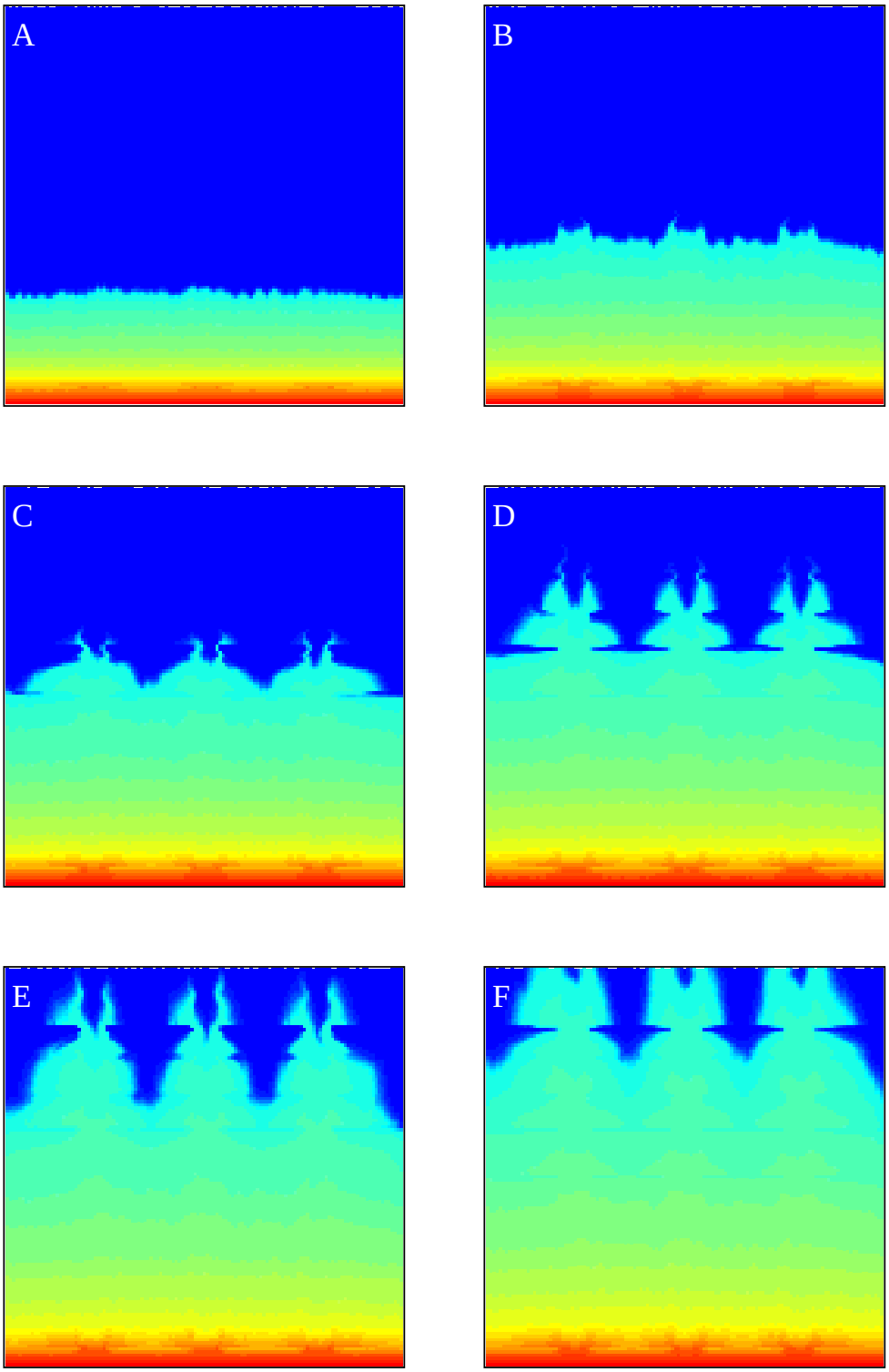

Fig.11(f) Snapshots of supercritical CO_2 and water flow in a region of turbidite beds with parallel, discontinuous layering, with wave-like perturbations 2. The modelled region is 38 by 38m. CO_2 is injected along the bottom edge of the model which is initially water saturated. Constant flow boundary conditions with flow from bottom to top and no flow conditions imposed right and left. Tongues of high CO_2 saturation develop corresponding to anticlines in layering.

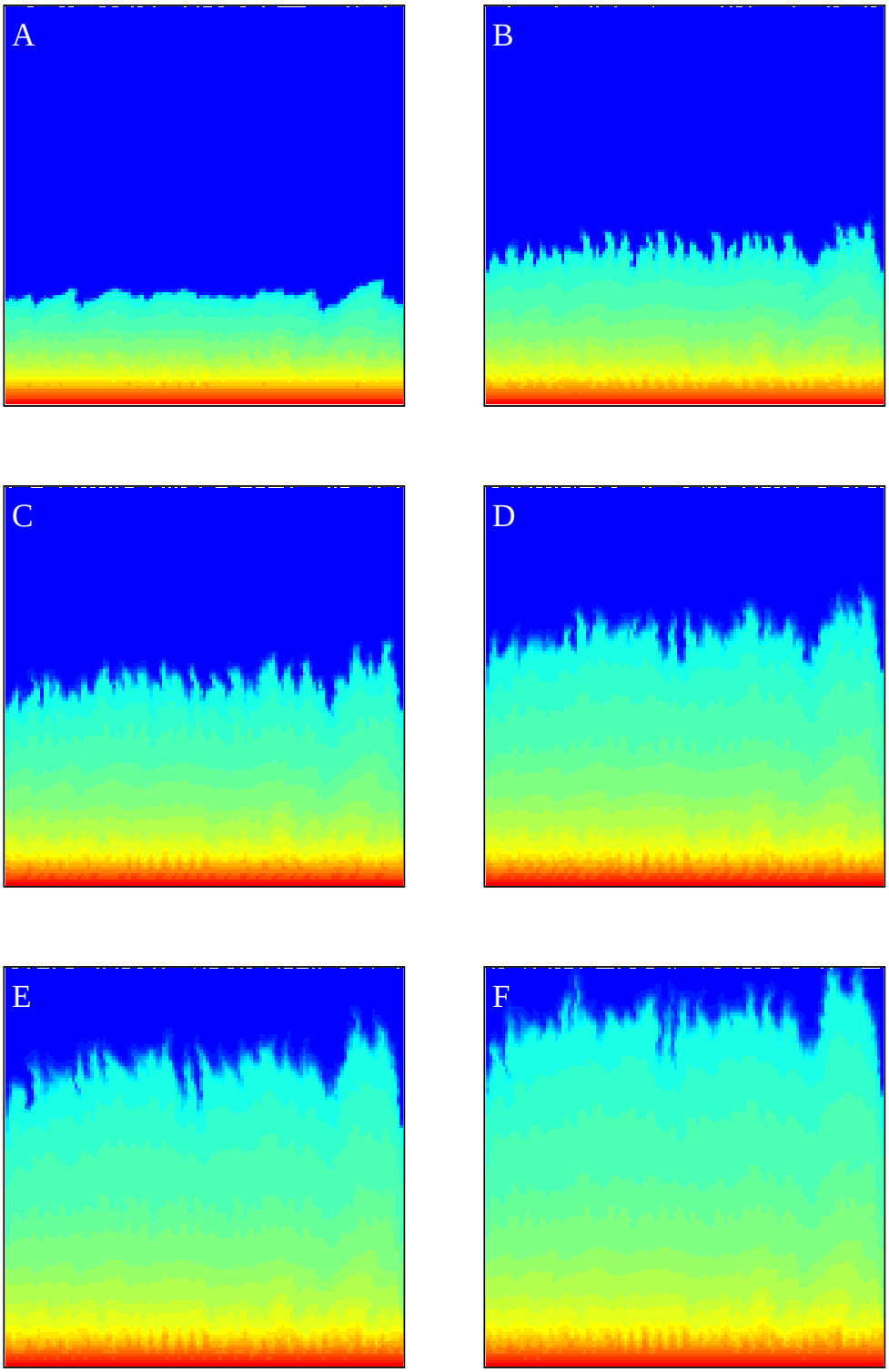

Fig.11(g) Snapshots of supercritical CO_2 and water flow in a region of cross-bedded sandstone. The modelled region is 0.5 by 0.5m. CO_2 is injected along the bottom edge of the model which is initially water saturated. Constant flow boundary conditions with flow from bottom to top and no flow conditions imposed right and left. Some fingering is developed but otherwise the saturation field resembles that of homogeneous sands.

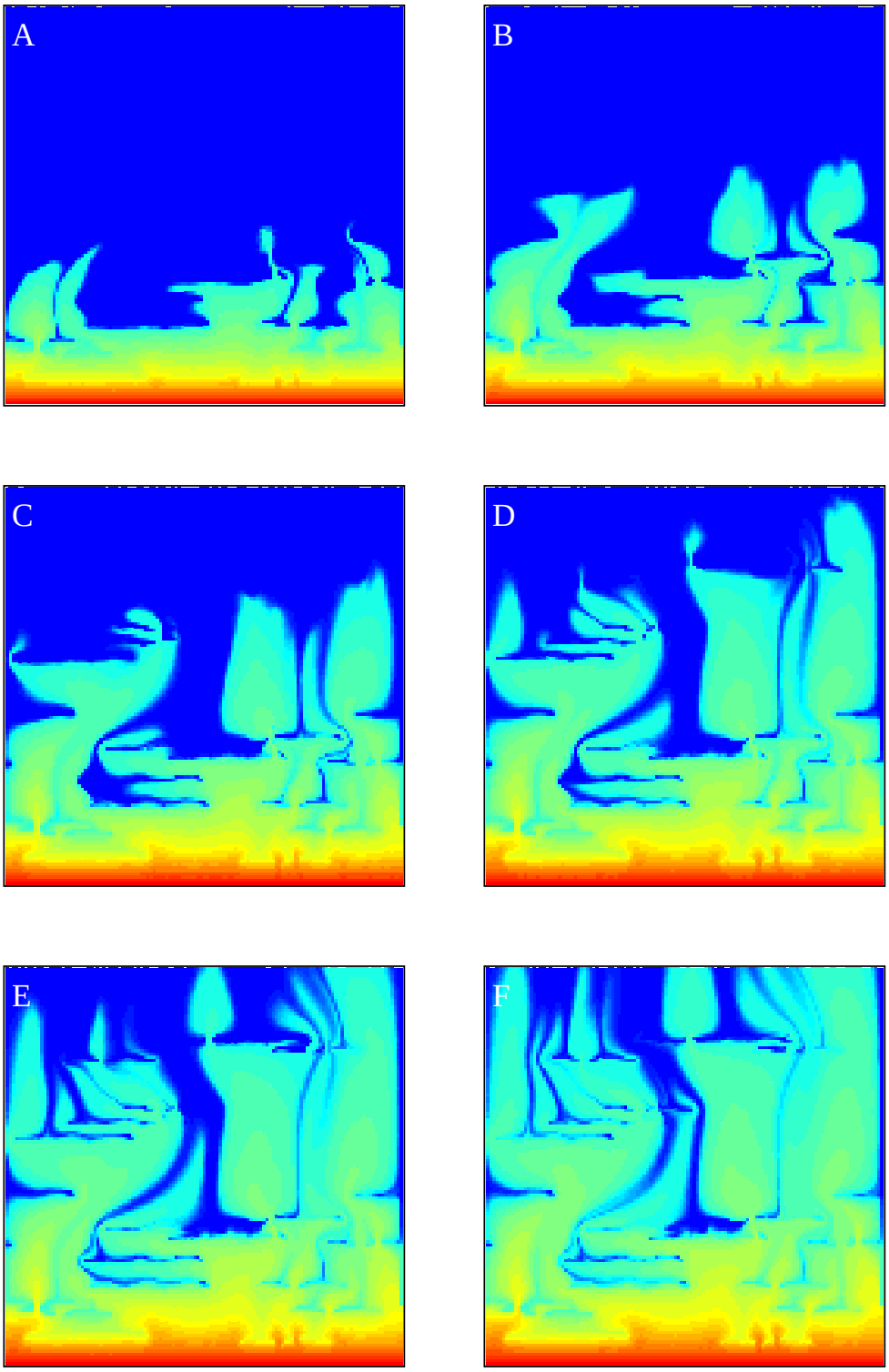

Fig.11(h) Snapshots of supercritical CO_2 and water flow in a region of massive sands with fluid escape structures. The modelled region is 0.6 by 0.6m. CO_2 is injected along the bottom edge of the model which is initially water saturated. Constant flow boundary conditions with flow from bottom to top and no flow conditions imposed right and left. Highly heterogeneous saturation fields are developed.

Saturation evolution plots

One way of examining changes in the heterogeneity of the saturation field with time is to plot the saturation variation along the outflow boundary for each time step. In Fig 12, these 'saturation evolution' plots are shown together with the average saturation for the outflow boundary (equivalent to a 'breakthrough' curve for contaminant transport), for the seven cases with flow perpendicular and parallel to the layering.

For the case of parallel continuous layering in turbidite sequences (Fig.12(a)), the plot for flow perpendicular to layering simply shows the arrival of a planar front and a gradual increase in saturation, very similar to the matrix only case. Saturations at a given time are slightly higher than in the matrix only case, indicating that the presence of low permeability layers tend to 'hold up' the front resulting in greater saturations when they arrive at the outflow boundary. When flow is parallel to the layering (Fig.12(a)), the high permeability layers are free to form rapid channel ways for injected CO_2 which arrives first at the out-flow boundary. It can be seen that even in the lowest permeability layers flow occurs and CO_2 saturation increases, although more slowly, with time. These effects give a marked striped appearance to the plot.

In the case of parallel finite layering in turbidite sequences (Fig.12(a)), the arrival of CO_2 at the boundary is spread over a longer time period, and shows relative delay at the left hand edge of the model. Here irregularities in the front are on the scale of the whole model, following the lengths of the discontinuous layering. For flow parallel to layering (Fig.12(a)), the picture looks similar to that for parallel continuous layering with CO_2 reaching the boundary first along the high permeability layers. For the case of continuous layering with perturbations (Fig.12(b)), the break-though pattern records the arrival of the two sets of fingering seen in the snapshots giving a wave-like form to the break-through pattern.

In the case of cross-bedding (Fig.12(c)), the patterns for flow both perpendicular and parallel to layering show similar patterns. This is because the layering of permeability contrasts is 45 deg to the bedding resulting in similar behaviour for these two directions. Both patterns are similar to the matrix only case except that fingering is slightly more pronounced. In the case of fluid escape structures (Fig.12(c)), flow parallel to layering shows a planar front with small sections that show delay, corresponding to the positions of the dish structures. When flow is perpendicular to the layering, arrival of CO_2 at the outflow boundary is spread over a larger time range and is more irregular. The plot has a stripped appearance showing the presence of narrow bands of reduced CO_2 saturation that are also visible in the snapshots.

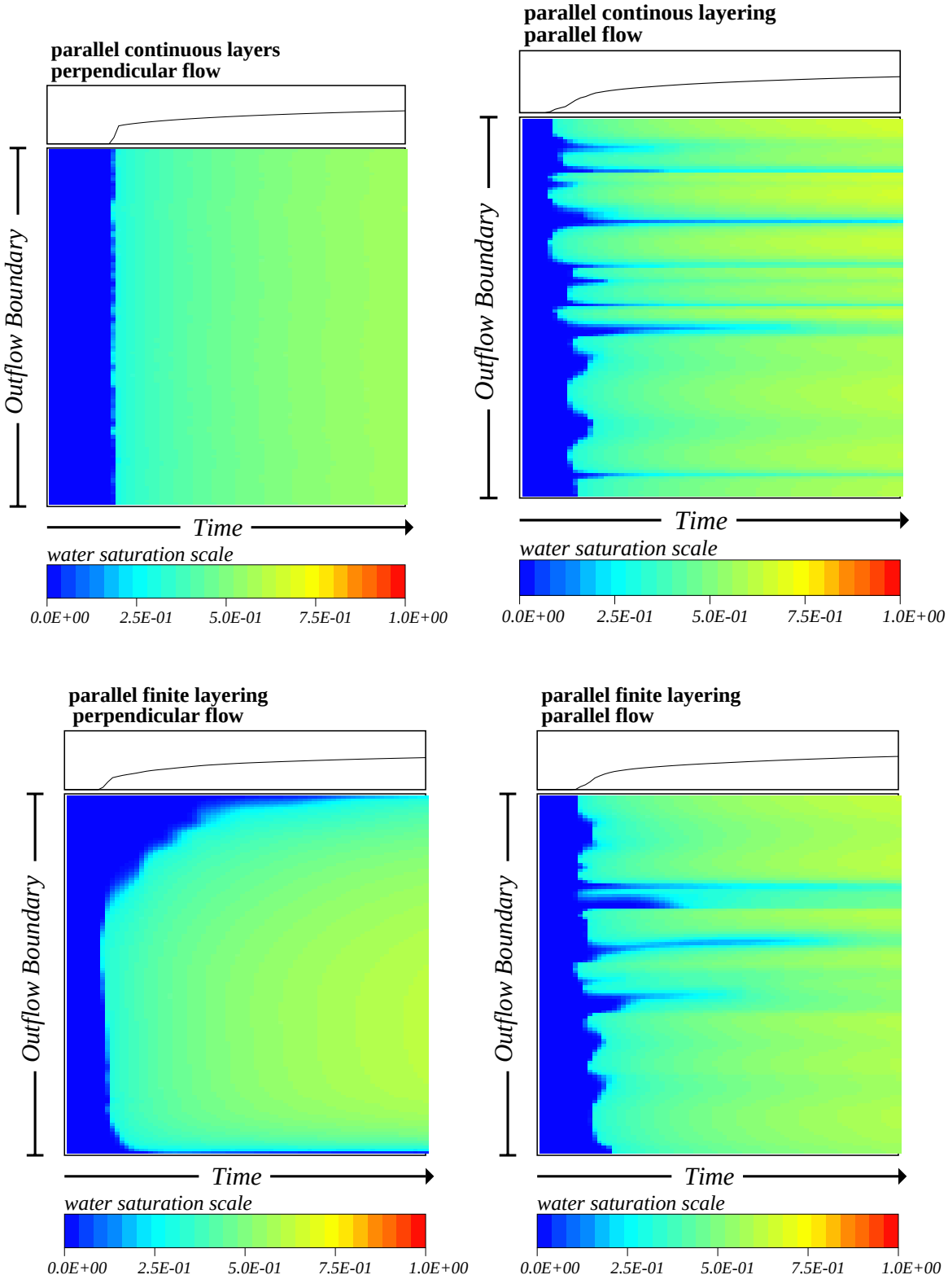

Fig.12(a) Saturation evolution plots showing the changes in the saturation at the boundary with time through the simulations. Top – turbidite sequence with parallel continuous layering with flow perpendicular (left) and parallel (right) to layering. Bottom - turdidite sequence with parallel discontinuous layering (shale layers around 5m long) and flow perpendicular (left) and parallel (right) to layering.

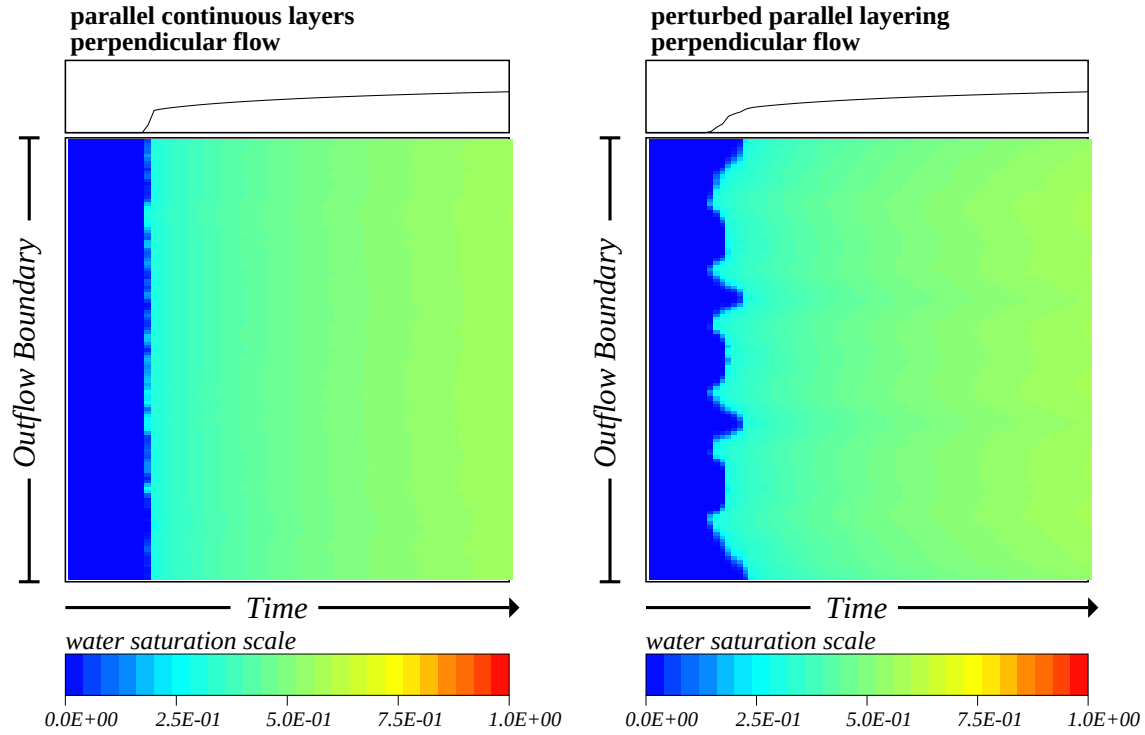

Fig.12(b) Saturation evolution plots showing the changes in the saturation at the boundary with time through the simulations. Left – turbidite sequence with parallel continuous layering. Right - turbidite sequence with parallel continuous layering and wave-like perturbations.

Pseudo curves and sensitivity analysis

The output saturation fields at each time step are used to determine 'pseudo' relative permeability curves, representative of the whole modelled region, using the method of Kyte and Berry (1975) outline in the previous section. Here the flows of CO_2 and water at the outflow boundary at each time step are used to determine representative values of relative permeability to supercritical CO_2 and water. These are plotted against the saturation of the whole model to give 'pseudo' relative permeability curves representative of the whole modelled region. For each heterogeneity case, a series of ten realizations with inflow along one boundary was made to test the sensitivity of the resultant curves to heterogeneity geometry.

In Fig 13(a), the pseudo relative permeability curves and saturation versus pore volume injected for the cases of turbidite layering (continuous and discontinuous) where flow is perpendicular to the layering are shown. It can be seen that the case of parallel continuous layers gives curves very similar to those for matrix and that the curves for the ten realizations are very similar. The only difference from the matrix only case, is that saturation increases more rapidly for pore volumes injected. This is due to the 'compression' of the CO_2-water front caused by the presence of low permeability layers, as discussed above. By contrast, the case of parallel discontinuous layering shows a wide scatter of relative permeability curves that show shallower slopes and migration of the cross-over point to lower saturation values. The curves for saturation versus pore volumes injected also show a wide scatter. It is clear that in this case, a 'representative area' for which constant curves can be expected, has not been reached and must be larger than the model presented (38 by 38 m).

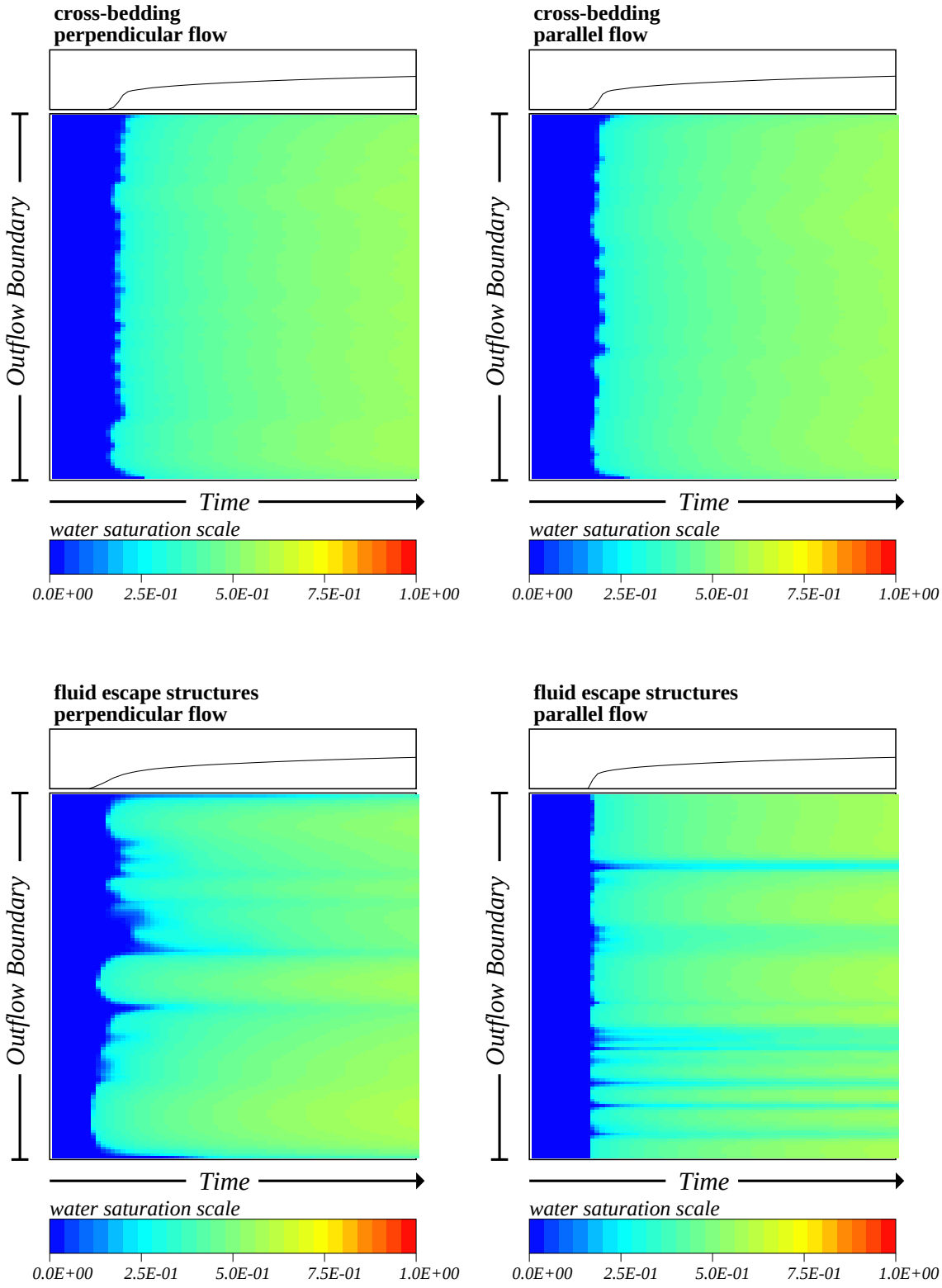

Fig.12(c) Saturation evolution plots showing the changes in the saturation at the boundary with time through the simulations. Top – cross-bedding with flow perpendicular (left) and parallel (right) to layering. Bottom – massive sands with fluid escape structures with flow perpendicular (left) and parallel (right) to layering.

The plots for the case of flow parallel to the layering are shown in Fig.13(b). Here the cases of continuous and discontinuous layering give similar results for relative permeability curves. The curves for saturation versus pore volumes injected show that saturation increases more slowly for the continuous than the discontinuous case. This is probably due to slightly lower proportion of shales in the discontinuous layer case simulations.

Fig.13(c), show the effect of introducing perturbations into parallel continuous layering which is to produce some scatter in the curves although not a pronounced as in the case of discontinuous layering. Such perturbations also tend to reduce the rate at which saturation increases with fluid injection.

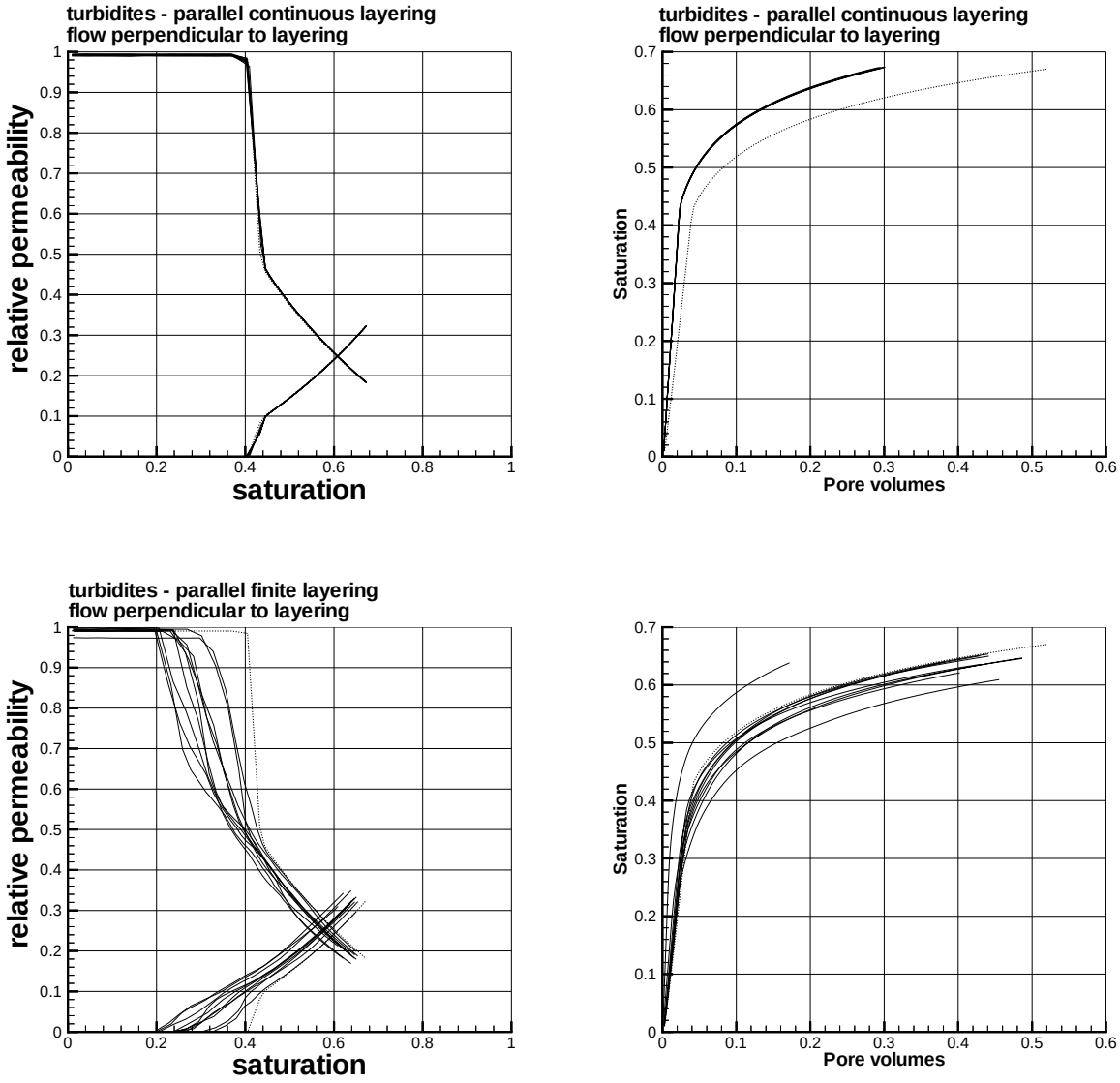

Fig.13(a) Pseudo relative permeability curves (left) and saturation versus injected pore volume of fluid (right). Top – turbidite sequence with parallel continuous layering. Bottom - turbidite sequence with parallel discontinuous layering (shales around 5m long). Dotted line – case for homogeneous sands.

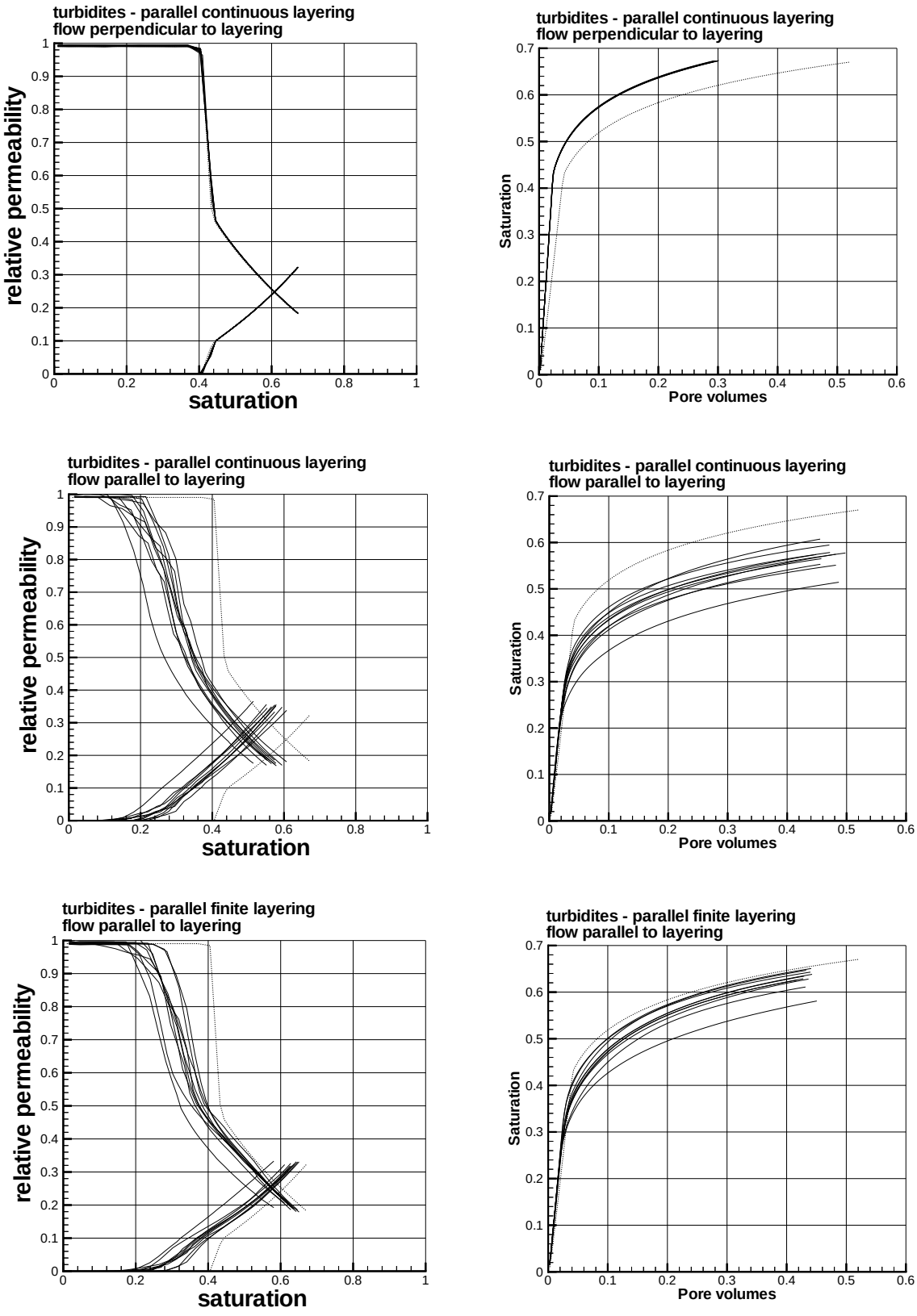

Fig.13(b) Pseudo relative permeability curves (left) and saturation versus injected pore volume of fluid (right). Top – turbidite sequence with parallel continuous layering, flow perpendicular to layering. Centre – turbidite sequence with parallel continuous layering, flow parallel to layering. Bottom - turbidite sequence with parallel discontinuous layering and flow parallel to layering. Dotted line – case for homogeneous sands.

The case of matrix only (Fig.11(a)) shows a simple picture of the CO_2-water front moving as a line parallel to the injection edge across the modelled area. The random variations in permeability of one half order of magnitude cause small scale fingering that is most evident in the last snapshot. Due to the high viscosity ratio, the front is highly smeared out with most of the model in the last snapshot having saturation of less then 0.5.

The case of continuous parallel turbidite layers (Fig.11(b)) shows a very similar picture to the matrix only case. This is because the layering is perfectly parallel, perpendicular to the pressure gradient. However, for the two cases of discontinuous layering (Fig.11(c) and (d)) there are marked changes with highly complex saturation fields developing as the injected CO_2 flows round the low permeability shale layers. This produces large contrasts in saturation with areas of trapped water where flow rates are very slow and thin tongues of CO_2 reaching out into the water saturated region.

The two cases of perturbed layering (Figs.11(e) and (f)) show that even small deviations from perfectly planar and parallel layering have significant effects on the flow patterns. The 'high' points or anticlines in the perturbations are places of preferential flow and the 'corners' where there are steps in the layering give rise to secondary tongues of increase CO_2 saturation. These effects increase as the CO_2 front moves through the model area being magnified at each low permeability layer crossed. The geometry of the perturbations is reflected in the frequency and the spacing of the CO_2 tongues as is seen by comparing the two examples.

The case of cross-bedding (Fig.11(g)) is similar to the case of matrix only in that the CO_2 front advances as an approximately straight line perpendicular to the pressure gradient. However, the fingering effects are enhanced compared to the matrix only case. The effect of the different directions of cross-beds is seen in the thick bed near the base of the model but these effects appear to average out over the rest of the model to produce fingering parallel to the pressure gradient.

The case of fluid escape structures (Fig.11(h)) show the most complex saturation field of all the models. The thin dish structures act as discontinuous flow barriers so this case resembles, in part, the discontinuous turbidite sequence case but with shorter low permeability layers. The fluid escape pipes form pathways of high flow which generated small CO_2 plumes at their low pressure ends. As CO_2 flows round the dish structures and along the fluid escape pipes, it leaves areas of high water saturation trapped behind the front creating highly complex and variable saturation fields.

For the cases of small scale heterogeneities, the case of cross-bedding (Fig.13(d)) shows similar results to the matrix only case with minor scatter introduced. However, the rate of saturation increase is slightly enhanced over the matrix case. Fluid escape structures produce a scatter similar to that for discontinuous layering with a similar migration of the cross-over to lower saturations. The rate at which saturation increases is slightly lower than the matrix only case. From the scatter, it is clear that the model area of 0.6 by 0.6 m is not large enough to be representative.

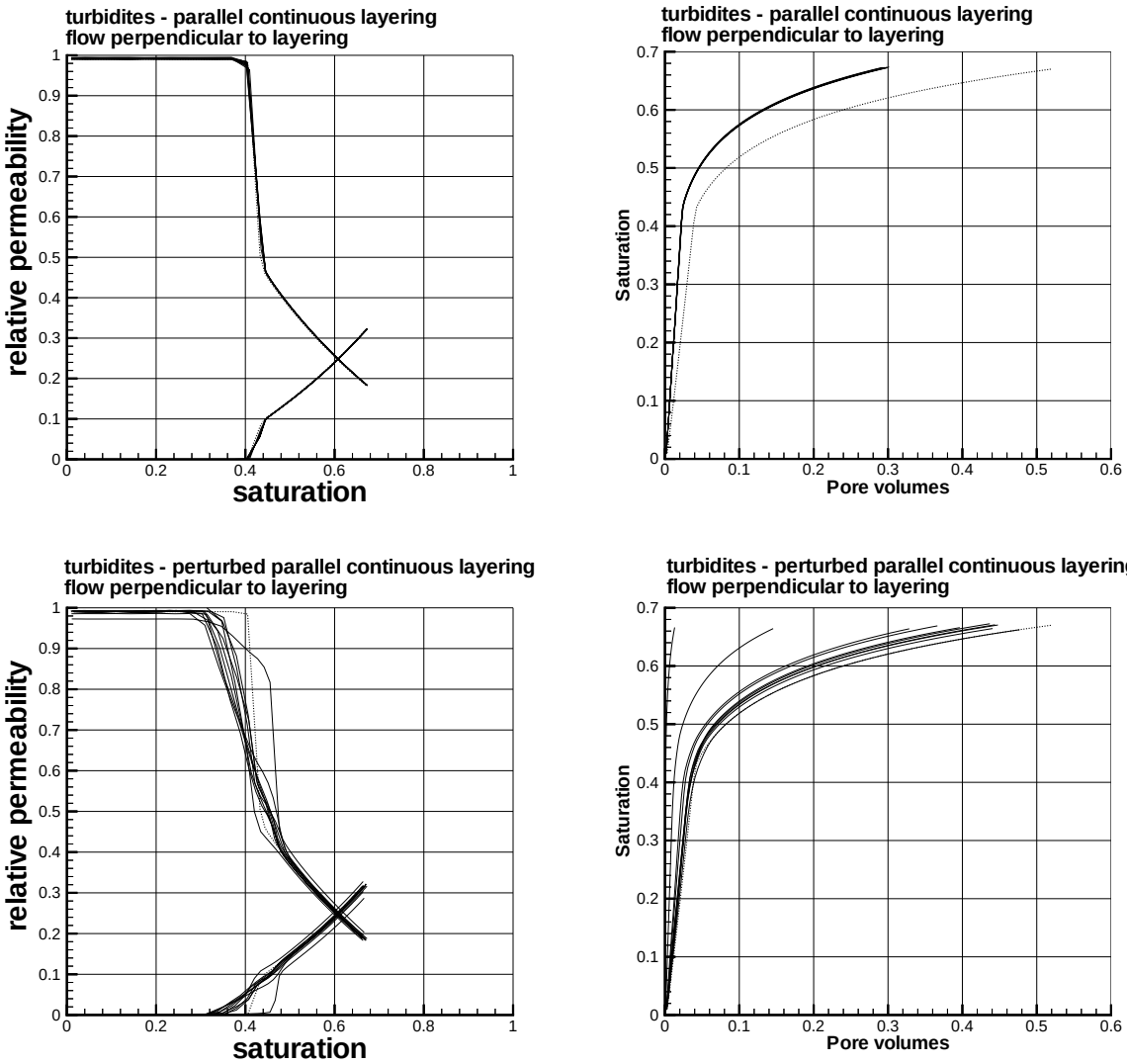

Fig.13(c) Pseudo relative permeability curves (left) and saturation versus injected pore volume of fluid (right). Flow perpendicular to layering. Top – turbidite sequence with parallel continuous layering. Bottom - turbidite sequence with parallel continuous layering and wave-like perturbations.

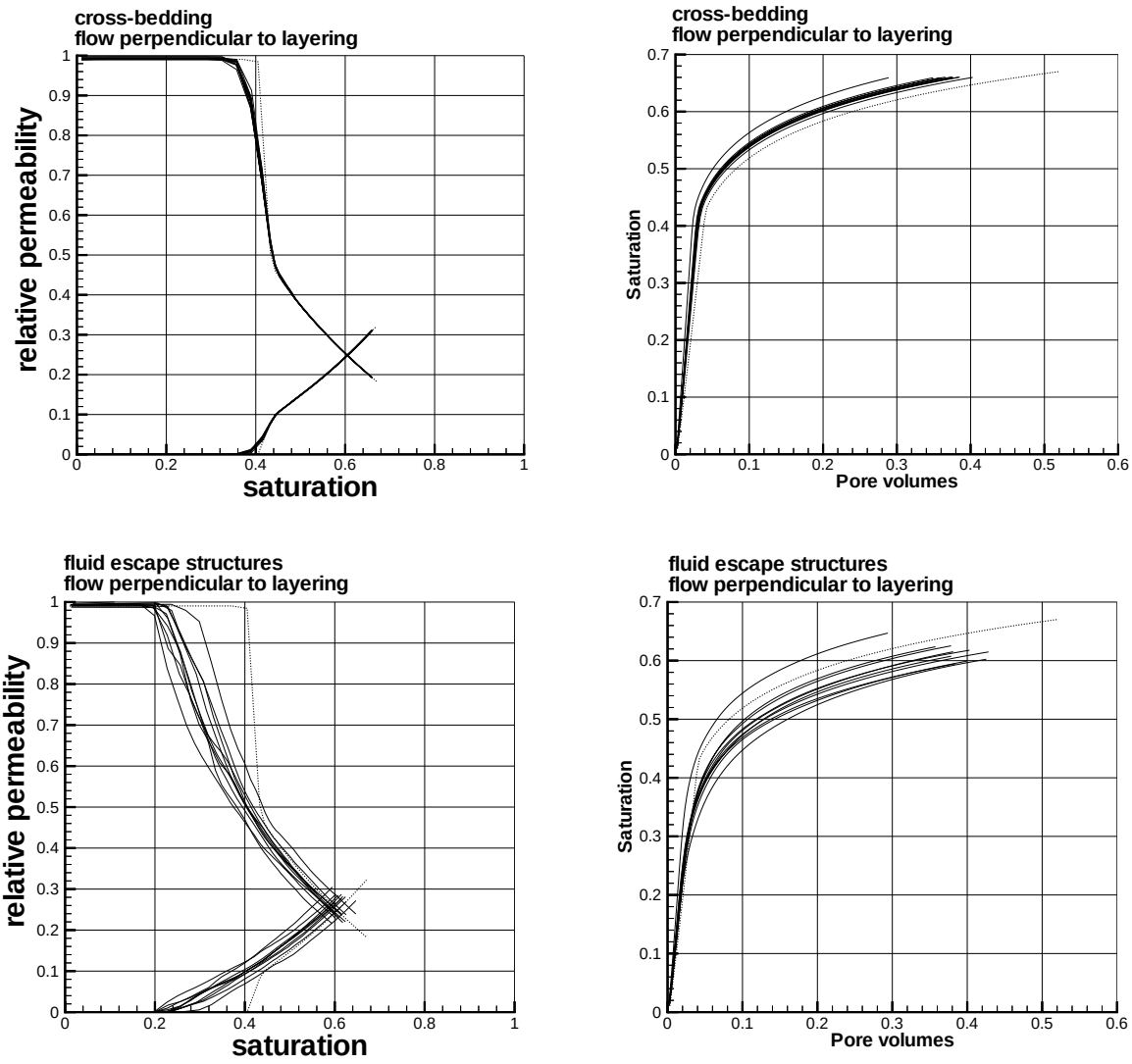

Fig.13(d) Pseudo relative permeability curves (left) and saturation versus injected pore volume of fluid (right). Top – cross-bedding with flow perpendicular (left) and parallel (right) to layering. Bottom - – massive sandstones with fluid escape structures with flow perpendicular (left) and parallel (right) to layering.

Discussion and Summary

At present there is very little information available on the nature of the sediments of the Utsira Sand and the Utsira Formation. There have been varying interpretation of the depositional environment from shallow to deep water conditions but recent work on seismic sections (Gregersen 1997, Lothe and Zweigel 1999, Torp 1999) suggest that the Utsira Formation may represent a sub-marine fan complex. As such, the sediments can be expected to be heterogeneous and contain internal sedimentary structures on the scale of cm to km. The most common of these could include, on the scale of 10s to 100s m, turbidites with sand beds of varying grain size and sorting, and shales of differing lengths and continuity. On a smaller scale (10s cm to 1m), features such as cross-bedding and fluid escape structures can be expected. Although the Utsira Sand where CO_2 is currently being injected is thought to be dominated by sands, there is evidence that it contains a number of shale layers which may extend laterally by as much as 2 km. Due to the limited resolution of the available data, it is possible, and indeed probable, that this unit contains many additional shales thinner than 1 m of unknown lateral extent.

Seven cases of sedimentary heterogeneity likely to occur in the sediments of a sub-marine fan complex have been investigated for their impact on supercritical CO_2 migration and dispersion using a two-phase flow model. Representative permeability and porosity fields have been generated using the coupled Markov chain method together with information from sediment analogues and the permeability of weakly to unconsolidated sands and shales/clays from the literature. This model can produce, using information from logs and maps, any number of stochastic realizations of a heterogeneous field that possess the same spatial characteristics.

The simulation of the saturation evolution during CO_2 injection shows how the nature of layering (bedding) affects CO_2 migration. For flow perpendicular to layering, where sand and shale layers are perfectly parallel flow behaves similarly to a that in a homogeneous sand. However, small i deviations from this simple pattern has large consequences for the nature of the saturation field. In fact, the simple picture of perfectly parallel layers is very unrealistic as, in nature, shale and sand layers are discontinuous and due to erosion events, differential compaction rates and faulting, layers are not perfectly planar. The flow simulations show that discontinuous shale layers produce highly heterogeneous saturation fields and complex fluid fronts.

Wave-like perturbations give rise to fingering (tongues of CO_2) on the same wavelengths as that of the perturbations. On a smaller scale, the permeability contrasts expected in cross-bedded sands did not greatly affect the heterogeneity of the saturation field but the presence of fluid escape structures (dish structures and fluid escape pipes) can produce highly heterogeneous saturation fields. Thus the presence of thin discontinuous low permeability layers, which has little impact on the global permeability, can have large effects on the two phase flow properties.

The simulations suggest that heterogeneities on a wide range of scales can insignificantly impact on the migration and dispersion of injected CO_2. The flow model results have been quantified through the determination of pseudo relative permeability curves for blocks of heterogeneous sediment. These curves can be used as input parameters to large scale multi-phase flow models to up-scale heterogeneities on a scale below the resolution of the model. The pseudo curves (Fig.13) show generally, that as the level of permeability heterogeneity increases, the slope of the pseudo curves decreases and the cross-over between curves for water and supercritical CO_2 migrates to the left (to lower saturations). Pseudo curves are different for flow perpendicular and parallel to layering,

particularly when the layering reflects large contrasts in permeability. As heterogeneity increases, the rate at which the CO_2 saturation in the modelled region increases with pore volumes of injected CO_2 is reduced.

Model results for ten realizations for each heterogeneity case show that the level of heterogeneity also affects the reproducibility of the pseudo curves. In addition curves are different for flow perpendicular and parallel to layering. The variations in the resulting pseudo curves indicate that the size of the representative elementary volume (REV) for two phase flow has not been reached in these cases. The REV is defined as the minimum volume for which small changes in size and location result in only small changes in two-phase flow properties. In the case of layering with strong permeability contrasts (like inter-bedded sands and shales/clays or dish structures) the REV will only be reached when the length of the shale layers is small compared to the volume considered.

While in the case of fluid escape structures, a volume of some 5 to 10 m across may be sufficient to satisfy this condition, shale layers have a probable wide range of possible lengths, possibly up to 2 km (Lothe and Zweigel 1999). In this case, it is obvious that a meaningful REV does not exist. As an alternative, a stochastic approach may be adopted where pseudo curves are allowed to vary over the large scale flow model in an attempt to incorporate the effect of heterogeneities in a meaningful fashion.

It can be seen from the 'snapshot' saturation fields that there is noticeable, although much lower, flow in the shales compared to the sands. In running the two-phase flow program it was found that up to 4 orders of magnitude contrast in permeability could be managed. The program at present cannot handle zero permeability. The shales in the turbidite sequences were assigned a value of 0.05mD and the clay layers in dish structures, 0.2mD. These values lie at the top end of the possible range of shale/clay permeabilities at reservoir conditions (0.01 to 1.0e-06 mD) and thus the model maximizes the possible role of the shales in conducting flow.

The two-phase flow program used here does not take capillary pressure into accounts. There may therefore be some effects which are not captured by the presented model results. In addition, the two-phase flow model does not model the effects of take gravity. Close the injection point, flow of CO_2 is probably dominated by the pressure gradient between the injected fluid and reservoir conditions. However, far from the injection point the migration of CO_2 will be driven by the density difference between water and CO_2 which causes CO_2 to rise. In the laterally unconfined conditions of the aquifer this can be expected to lead to more pronounced flow parallel to layering than is shown by the snapshots of the saturation fields in Fig.11, as CO_2 spreads sideways under the low permeability shale layers.

The permeability of shales remains one of the greatest uncertainties in the modelling. It is now thought that shales always have non-zero permeability (Neuzil 1994) and thus cannot form a complete seal for infinite lengths of time. Shale permeability depends on clay mineralogy, internal structure, depth and fluid chemistry and can vary by several orders of magnitude at any depth. In the short term (days, months) permeability contrasts between shales and sands mean that flow is dominated by the more permeable sands. However, in the long term (years), ponds of CO_2 will build up under the cap rock of the Nordland shales and under shale layers within the Utsira Sand generating pressure gradients. The permeability of the shales will then determine the length of time they can act as an efficient seals. With the information presently available on the hydraulic properties of the shales, this remains largely unknown.

The main conclusion from the modelling is that heterogeneities which are very likely to be present in the Utsira Formation will have a significant effect on the migration of injected CO_2. This has been confirmed by the comparison of the recent seismic survey and a survey taken before injection began which indicates that already injected CO_2 is present in a wide region reaching the height of the Utsira Sand (200 m) and over twice as broad (500 m). This compares with early simulations by IKU (Torp 1999) of the CO_2 bubble using a homogeneous sediment which indicates a narrow column only some 50 m broad. Later models by IKU, however, where impermeable shale layers were included clearly show how shale layers can greatly increase the lateral migration of injected CO_2. The breadth of the CO_2 plume indicated by the seismic surveys can most likely be attributed to sediment heterogeneity. Such heterogeneity reduces the effective storage of the aquifer since saturation fields become heterogeneous with trapped pockets of water and increased the volume of low saturations. However, this increased dispersion of injected CO_2 could increase the rates at which CO_2 dissolves in the formation waters and reacts with the host sediments to become permanently stored. The modelling presented here has been used to generated pseudo relative permeability curves for flow perpendicular and parallel to layering (bedding) for blocks of heterogeneous sediment. These curves could be used as input to large scale flow models in order to include the effects of heterogeneities on scales below the size of a large scale simulator grid block. This may allow more representative simulations of the long term effects of CO_2 injection to the Utsira Formation.

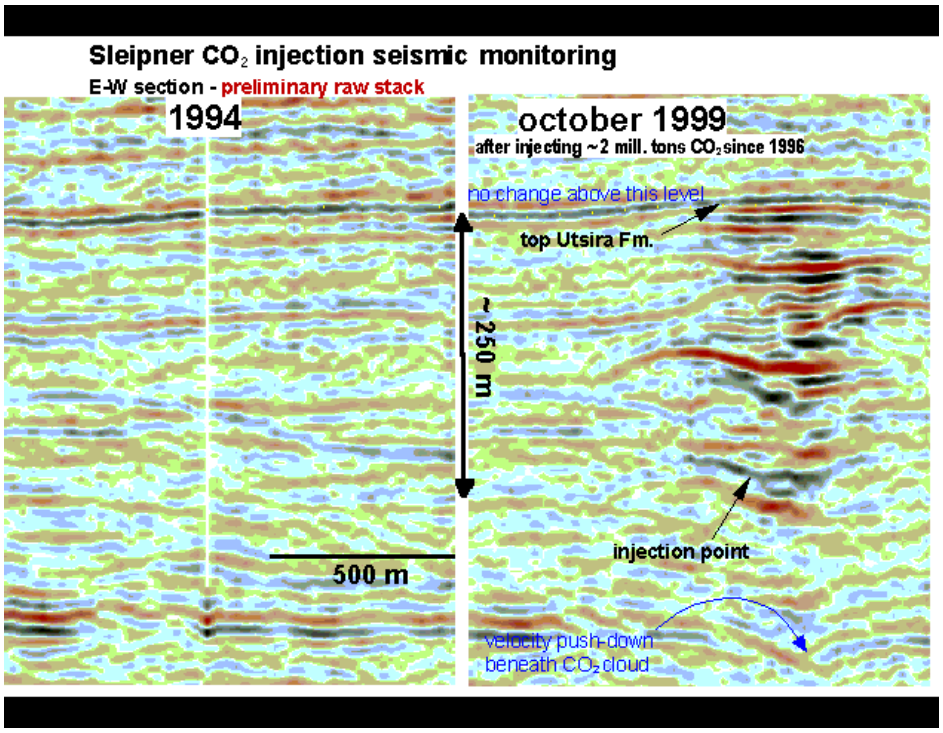

Fig.14 Comparison of seismic surveys before and 2 years after start of CO_2 injection. The CO_2 plume is about 200m high and 500m broad (recent results from SACS project).

Conclusions

The conclusions of the study are summarized below:

1) If the Utsira Formation is a sub-marine fan system, commonly occurring heterogeneities could include turbidite sequences of inter-bedded sands and shales/clays (10's m scale) showing discontinuous shale/clay layers and wave-like perturbations of layering, and small scale features (1 m scale) such as cross-bedding and fluid escape structures.

2) The largest impact of CO_2 migration is shown by turbidite sequences with discontinuous shale/clay layers but significant effects occur due to wave-like perturbations of layering geometry. The permeability contrasts expected in cross-bedding have a small effect only, but fluid escape structures can generate highly heterogeneous permeability fields. That heterogeneities can significantly affect the migration of injected CO_2 is confirmed by the recent comparison of seismic surveys which shows that the CO_2 plume is much broader than predicted for a homogeneous aquifer.

3) The effects of sediment heterogeneity are reflected in the nature of the relative permeability 'pseudo' curves. As heterogeneity increases, the slopes of curves become less steep and the cross-over point migrates left towards lower CO_2 saturations. The variations in the curves for stochastically similar simulations also increases. This indicating that the size of the REV is increasing and a meaningful REV may not exist for the case of discontinuous shale layers.

4) The presence of heterogeneities also results in a reduced rate saturation increase with pore volumes of CO_2 injected. The lower saturations and complex fluid fronts that result will promote dissolution of CO_2 into the formation waters and reaction with the host sediments.

References

Barker J.W. and Thibeau S. 1997: A critical review of the use of pseudo-relative permeabilities for upscaling. SPE Reservoir Engineering, May 1997.

Buller A.T., Johnsen S.O., Rueslåtten H., Rundberg Y. 1982 The Tertiary section in Block 30/6 (wells 30/6-1, 2, 3, 4) confidential report to Statoil, Geologisk Inst., NTH, Trondheim.

Bouma A.H. 1962 Sedimentology of some flysch deposits. Elsevier, Amsterdam, 168pp.

Clark J.D. 1995 Detailed section across the Ainsa II channel complex, south central Pyrenees, Spain. In: Pickering K.T., Hiscott R.N., Kenyon N.H., Ricci Licchi F. and Smith R.D.A.(Eds*) Atlas of deep water environments, architectural style in turbidite systems*. Chapman & Hall, London, 139-144.

Dake L.P. 1978: Fundamentals of reservoir engineering. Developments in Petroleum Science, 8, Elsevier, Amsterdam, 443pp.

Deegan C.E. and Scull B.J. 1977 A standard lithostratigraphic nomenclature for the Central and Northern North Sea, Report 77/25, Bull.1. Institute of Geological Sciences, London; Oljedirektoratet, Stavanger.

Dewhurst D.N. and Aplin A.C. 1998 Compaction-driven evolution of porosity and permeability in natural mudstones: an experimental study. J.Geophys. Res., 103(B), 651-661.

Eidvin T. and Riis F 1995 Neogen og øvre paleogen stratigrafi på norsk kontinentalsokkel (fra Ekofisk-feltet i sentral Nordsjøen til Bjørnøya-Vest i sydvestlige deler av Barentshavet), Oljedirektoratet, Stavanger, 144.

England W.A. MaKenzie A.S., Mann D.M., Quigley T.M. 1987 The movement and entrapment of petroeum fluids in the subsurface. J.Geol.Soc.Lond., 149, 327-347.

Elfeki A.M.M., Uffink G.J.M. and Barends F.B.J. 1997 Groundwater contaminant

Feder J. 1988: *Fractals*. Plenum Press, New York, 283pp.

Fetter C.W. *Applied Hydrogeology.* Merrill Publ. Company, Columbus, Ohio, 592pp.

Gregersen U., Michelsen O. and Sorensen J.C. 1997 Stratigraphy and facies distribution of the Utsira Formation and the Pliocene sequences in the northern North Sea. Marine and Petroleum Geology, 14, 893-914.

Gregersen U., Upper Cenozoic channels and fans on 3D seismic data in the northern Norwegian North Sea. Petroleum Geoscience 4, 67-80.

Heggland R. 1997 Detection gas migration from a deep source by use of exploration 3D seismic data. Marine Geology 137, 41-47.

Hurst A. 1991 Permeability variations in sandstones and their relationship to sedimentary structures. In: Lake L.W., Carrol H.B.Jr., Wesson T.C. (eds*) Reservoir Characterization II*, NPF, 167-196.

Hurst A. 1993 Sedimentary flow units in hydrocarbon reservoirs: some shortcomings and a case for high-resolution permeability data. Spec. Publ. Ass. Sediment 15, 191-204.

Isaksen D. and Tonstad K. 1989 A revised Cretaceuos and Tertiaty standard lithostratigraphic nomenclature for the Norwegian North Sea, NPD bull.5; Oljedirektoratet, Stavanger.

James A.M. and Lord M.P. 1992 *Macmillan's Chemical and Physical Data.* Macmillan, London.

Jordt H., Faleide J.I., Bjørlykke K., Ibrahim M.T. 1995 Cenozoic sequence stratigraphy of the central and northern North Sea Basin, tectonic development, sediment distribution and provenance areas. Mar.Petrol.Geol., 12, 845-879.

Gidman J., Schweller W.J., Reed A.A. 1993 Reservoir character of deep marine sandstones, Inglewood field, Los Angeles Basin. In: Rhodes E.G., Moslow T.F. (eds*) Marine Clastic Reservoirs, Examples and Analogues.*, 231-262.

Kyte J.R. and Berry D.W 1975: New pseudo functions to control numerical dispersion. SPEJ, August 1975, 269-275.

Langlo P. 1992: *Macrodispersion for two-phase flow in heterogeneous media*. Ph.D. Thesis, University of Bergen, 101pp.

Morrow N.R., Huppler J.D., Simmons A.B. 1969 Porosity and permeability of unconsolidated, upper Miocene sands from grain size analysis. J. Sed. Geol., 39, 312-321

Lothe A., Zweigel P. 1999 Saline Aquifer CO_2 Storage (SACS). Annual report 1999 of SINTEF Petroleum Research's results in work area 1 "Reservoir Geology".

.Neuzil C.E. 1994 How permeable are clays and shales? Water Resour. Research 30, 145-150.

Odling N.E. 1997 Scaling and connectivity in a joint system in sandstones from western Norway. J. Structural Geology 19, 1257-1271..

Odling N.E. and Webman I. 1991 A conductance mesh approach to the permeability of natural and simulated fracture patterns. Water Resour. Res., 10, 2633-2643.

Reuil A. and Cathles III L.M. 1999 Permeability of shaley sands. Water Resour.Research 35, 651-662.

Pettersen Ø. 1990: *Grunnkurs i Revervoarmekanikk (Basic course in reservoir mechanics*) Publ. Univ. Bergen, Bergen, 103pp.

Pickering K.T., Hiscott R.N., Kenyon N.H., Ricci Licchi F. and Smith R.D.A.(Eds) 1995 *Atlas of deep water environments, architectural style in turbidite systems.* Chapman & Hall, London, 333pp.

Pickup G.E., Ringrose P.S., Forrester M.M., Jensen J.L. and Sorbie K.S. 1994: The geopseudo atlas: geologically based upscaling of multi-phase flow.SPE 27565.

Pickup G.E., Carruthers D. 1996 Effective flow parameters for 3D reservoir simulation. SPE 35495, April 1996.

Scheidegger A.E. 1974: *The Physics of Flow Through Porous Media*. Univ. Toronto Press

Schuppers J.D. 1993 Quantification of turbidite facies in a reservoir analogue submarine fan channel sandbody, south-central Pyrenees, Spain. Spec.Publ.Int.Ass. Sediment, 15, 99-112.

Sclater J.G. and Christie P.A.F. 1980 Continental stretching: an explanation of the post Mid-Cretaceous subsidence of the central North Sea basin. J.Geophys. Res., 85(B), 3711-3739.

Stow D.A.V. (Editor) *Deep water turbidite systems*. Blackwell Scientific Publications. Int. Assoc. Sedimentologists Reprint Series 3, 473pp.

Weber K.J., Eijpe R., Leijnse P., Moens C. 1972 Permeability distribution in a Holocene distributary channel-fill near Leerdam, The Netherlands. Geologie en Mijnbouw 51, 53-62.

Wadsley M.W. 1993 Thermodynamics of multi-phase equilibria in the CO_2-seawater system. Proceedings of the Second Int, Workshop on interaction between CO_2 and ocean, Tsukuba, Japan, June 1993, 88-110.

Walker R.G. 1978 Deep-water sandstone facies and ancient sub-marine fans: models for exploration for stratigraphic traps. AAGG 62, 932-966.

Torp T.(Editor) 2000 SACS - Saline Aquifer CO_2 Storage - final technical report.

Wilkinson I.P. 1999 The biostratigraphical and palaeo-ecological application of calcareous microfaunas from the Utsira Formation in Norwegian well 15/9-A23. BGS report WH99/124R.